Geoscience Frontiers 15 (2024) 101737

Contents lists available at ScienceDirect

Geoscience Frontiers

journal homepage: www.elsevier.com/locate/gsf

Research Paper

Two-step exhumation of Caucasian intraplate rifts: A proxy of sequential plate-margin collisional orogenies

William Cavazza [a,*], Thomas Gusmeo [a], Massimiliano Zattin [b], Victor Alania [c], Onise Enukidze [c], Sveva Corrado [d], Andrea Schito [e]

[a] Department of Biological, Geological, and Environmental Sciences, Univ. of Bologna, Italy
[b] Department of Geosciences, Univ. of Padua, Italy
[c] Institute of Geophysics, I. Javakhishvili State University, Tbilisi, Georgia
[d] Department of Sciences, Roma Tre University, Rome, Italy
[e] Department of Geology and Geophysics, Univ. of Aberdeen, United Kingdom

ARTICLE INFO

Article history:
Received 26 May 2023
Revised 21 September 2023
Accepted 27 October 2023
Available online 2 November 2023
Handling Editor: Kristoffer Szilas

Keywords:
Intraplate deformation
Far-field tectonics
Greater Caucasus
Structural reactivation
Terrane accretion

ABSTRACT

Intraplate structural deformation is diagnostic of tectonic stress regime changes linked to plate interactions and can result from superposed tectonic events whose single contributions are hardly distinguishable. In this paper, we present a set of integrated thermochronologic inverse models along a 140 km-long transect across the central Greater Caucasus and the adjacent Adjara-Trialeti fold-and-thrust belt of Georgia, two intraplate orogens produced by structural inversion of parallel continental rift zones located on the Eurasian plate. Our dataset allows to distinguish discrete and superposed deformation episodes and quantify their respective contributions to orogenic exhumation. The integration of (U-Th)/He analysis on apatite and zircon, fission-track analysis on apatite, and peak-temperature determinations (clay mineralogy, organic matter petrography, Raman spectroscopy) shows that structural inversion was punctuated by two incremental steps starting respectively in the latest Cretaceous and the mid-Miocene. Latest Cretaceous partial inversion of the Greater Caucasus is documented here for the first time and placed in a geographically wider context of coeval deformation. The two episodes of intraplate structural inversion, exhumation, and sediment generation are chronologically and physically correlated with docking of (i) the Anatolide-Tauride-Armenian terrane (Late Cretaceous - Paleocene) and (ii) Arabia (Miocene hard collision) against the southern Eurasian plate margin. Intraplate deformation in the Caucasian domain was triggered by far-field propagation of plate-margin collisional stress which focused preferentially along rheologically weak rift zones.

1. Introduction

Sequential juxtaposition of lithospheric terranes along active continental margins generates superposed strain sequences which progressively complicate the tectonic interpretation of past collisional events. How then to resolve the incremental nature of plate-margin deformation and terrane accretion? How is collisional stress partitioned between suture zones and inherited intraplate geological structures? Recognition of multiple episodes of superposed intraplate deformation is extremely difficult if not altogether impossible when later deformation has overprinted the signature of earlier tectonic episodes. The use of multiple low-temperature thermochronological techniques with different closure temperatures generates detailed time–temperature paths, thus resolving past deformation episodes which otherwise might go undetected. In this paper, we focus on the structural inversion of intraplate rift basins, considered as proxies of far-field stress-regime variations linked to plate geometries and interactions (Ziegler, 1987; Cloetingh, 1988; Ziegler et al., 1995; Turner and Williams, 2004; Sandiford and Quigley, 2009; Cloetingh et al., 2005; Raimondo et al., 2014; Stephenson et al., 2020).

The southern margin of the Eurasian plate has experienced repeated accretion of Gondwana-derived lithospheric terranes and is a natural laboratory for studying the relationship between plate boundary and intraplate processes, the cyclicity of tectonic activity, and the origin of intraplate stresses. To tackle these issues, we applied multiple thermochronometers and thermal maturity

* Corresponding author.
E-mail address: william.cavazza@unibo.it (W. Cavazza).

https://doi.org/10.1016/j.gsf.2023.101737

indicators to a 140 km-long transect across two inverted rift basins parallel to the active southern margin of Eurasia: the central Greater Caucasus (GC) and the eastern Adjara-Trialeti (AT) fold-and-thrust belts of Georgia. The study area is well suited as ongoing structural inversion is incomplete and has not yet obscured the signature of previous collisional episodes. The results define for the first time two discrete and superposed episodes of intraplate exhumation/cooling correlated with well-established plate-margin collisional events, thus delineating a complex history of plate-margin deformation, collisional stress transfer, and localized intraplate structural reactivation.

2. Geological setting

The Greater and Lesser Caucasus (Fig. 1) constitute the most deformed portion of the hinterland of the 2,400-km-long Arabia-Eurasia collision zone. Head-on collision and deep indentation of the Arabian plate has caused widespread exhumation of deep-seated basement rocks along the Bitlis suture of southeastern Anatolia (Hempton, 1985; Okay et al., 1985, 2010; Oberhänsli et al., 2010; Cavazza et al., 2018) and has also promoted deformation across a wide swath of the upper (Eurasian) plate, where the reactivation potential of preexisting intra-plate crustal discontinuities has played a crucial role in focusing far-field collisional stresses (Vincent et al., 2007, 2011, 2020; Avdeev and Niemi, 2011; Albino et al., 2014; Cavazza et al., 2017, 2019; Vasey et al., 2020; Corrado et al., 2021; Gusmeo et al., 2021, 2022; Forte et al., 2022; Trexler et al., 2022).

The *Greater Caucasus* (GC) is considered the result of the Cenozoic structural inversion of a former back-arc basin that opened during the early Mesozoic in the Eurasian lithosphere above the north-dipping subduction of the Neotethys under the Lesser Caucasus magmatic arc (e.g., Zonenshain and Le Pichon, 1986; Mosar et al., 2010, 2022; Adamia et al., 2011; Ismail-Zadeh et al., 2020). The actual size and degree of extension of the Mesozoic basin, as well as the timing of its inversion and the overall exhumation pattern, are a matter of debate. In one end-member model (the *rift inversion model*), the GC basin was a relatively narrow continental rift underlain by continental crust and the orogen, after rift inversion, propagated towards the northern and southern forelands in a thin-skinned fashion (Nikishin et al., 2001, 2011; Mosar et al., 2010, 2022; Vincent et al., 2016, 2018). In the other (the *collisional model*), the basin was at least ca. 250 km wide and floored by oceanic or highly extended continental crust (Mumladze et al., 2015; Cowgill et al., 2016, 2018; Tye et al., 2020; Trexler et al., 2022). The available thermochronologic data constraining the exhumation pattern of the GC are reviewed in the following chapter.

The GC basin fill is mostly composed of marine sedimentary rocks of Jurassic-Cretaceous age, with largely predominant shales and fine-grained sandstone turbidites. Total thickness of the GC basin fill is in excess of 10 km; a volcanic/volcaniclastic component is present in the western portion of the orogen (Adamia et al.,

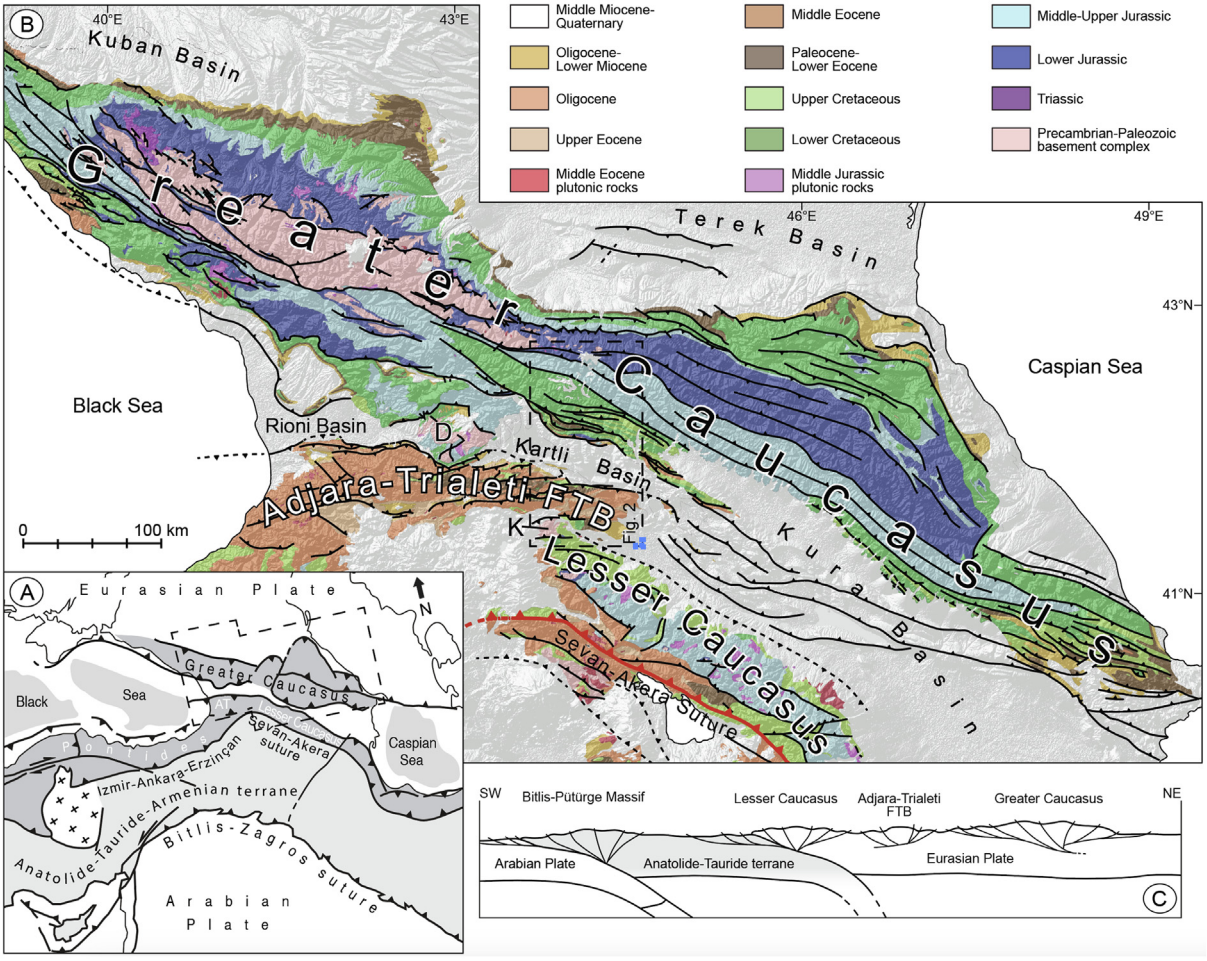

Fig. 1. (A) Sketch map of the Arabia-Eurasia collision zone (after Sosson et al., 2010). AT = Adjara-Trialeti fold-and-thrust belt. (B) Geological sketch map of the Caucasian region (from USSR 1:200,000 scale geological maps). Dashed rectangle indicates location of Fig. 2. D = Dzirula Massif, K = Khrami Massif. (C) Cross-section showing schematically the geodynamic setting and the tectonic relationships among the various domains.

2011) where Jurassic basalts have been portrayed as being emplaced within a narrow transtensional basin (Adamia et al., 1981). Exhumed basement units thrust southward characterize the GC western and -subordinately- central portions, whereas no basement is cropping out to the east, where only inverted basin-fill units are present. The GC is largely asymmetrical, with predominant south-vergent structures, particularly in its western and central segments (Adamia et al., 2010; Mosar et al., 2010, 2022). The eastern part of the GC is more symmetrical (e.g. Sobornov, 2021).

The deep structure of the GC is inadequately known. Relatively rare sub-crustal (<150 km deep) earthquakes have been interpreted as the result of the occurrence of an oceanic slab of limited extent beneath the eastern GC (Mumladze et al., 2015). Such conclusion conflicts with seismic tomographic data pointing to extensive lithospheric delamination (Koulakov et al., 2012; Zabelina et al., 2016). Widespread Late Pliocene-to-Quaternary volcanism occurred in the GC western-central part at Mt. Elbrus, the highest peak in Europe at 5,642 m, and at Mt. Kazbek in our study area (Fig. 2). Such volcanism is part of scattered magmatic displays across a vast area of the Arabia-Eurasia collision zone and, based on a combination of geochemical, seismic and geodynamic constraints, has been interpreted as the result of small-scale convection associated with mantle upwelling (Bewick et al., 2022).

Progressive growth of the GC orogenic wedge has induced substantial lithospheric flexure on both sides of the orogen, with subsidence and tectonic progradation both southward (Rioni-Kartli-Kura basin) and northward (Kuban-Terek basin) (Fig. 1). The Rioni-Kartli-Kura composite basin (Fig. 1) has experienced pulses of flexural subsidence from opposing directions: Oligocene depocenters are aligned along its southern margin close to the Lesser Caucasus orogen while Neogene depocenters are located along its northern margin adjacent to the GC (Nemčok et al., 2013). Fault-plane solution data from the Rioni-Kartli-Kura basin indicate ongoing north–south-oriented compression and convergence rates progressively increasing eastward up to 12 mm/yr (Reilinger et al., 2006; Forte et al., 2013, 2014). The Kuban-Terek basin to the north of the GC shows marked along-strike variations: its eastern part was affected by significant subsidence from the Oligocene and is bounded to the south by a well-developed north-verging frontal wedge whereas the western part underwent much less subsidence and shows a poorly developed frontal wedge (Ershov et al., 2003; Sobornov, 2021).

Located between the Greater Caucasus to the north and the Lesser Caucasus to the south, the *Adjara-Trialeti fold-and-thrust belt* (ATFTB) of western Georgia (Fig. 1) is the result of the structural inversion of a former back-arc basin which experienced most subsidence and extension in the middle Eocene, when a > 5,000 m thick volcano-sedimentary succession was deposited coevally with rifting in the eastern Black Sea (Robinson et al., 1996; Banks et al., 1997; Adamia et al., 2011; Tari and Simmons, 2018). Striking west-east, the ATFTB spans > 300 km (Fig. 1) from the Black Sea coast, where it continues offshore in the so-called Gurian fold-belt (e.g. Tari and Simmons, 2018), to Tbilisi, where it plunges eastward underneath the highly deformed Oligocene-to-Miocene sedimentary rocks of the Kura basin fill. The width of the orogen increases progressively westward. Likewise, the Middle Eocene *syn*-rift section thickens toward the Black Sea coast, where volcanic/ hypabyssal rocks are most abundant (Okrostsvaridze et al., 2018), thus pointing to the Adjara-Trialeti basin as an offshoot of the eastern Black Sea.

The age of the pre-rift succession of the ATFTB ranges from the late Early Cretaceous to the Early Eocene. Aptian-Cenomanian volcanics/volcaniclastics have been interpreted as connected to the Eastern Pontides-Lesser Caucasus subduction-related magmatic arc (Adamia et al., 1992, 1981; Yılmaz et al., 2014). During the Paleocene-early Eocene, the Adjara-Trialeti basin experienced flexural subsidence in the foreland of the Erzinçan-Sevan-Akera orogen and the deposition of a thick succession of terrigenous turbidites (Adamia et al., 2011; Banks et al., 1997; Yılmaz et al., 2014, 2000; Gusmeo et al., 2021). Back-arc rifting occurred in the Middle Eocene, as shown by a thick succession of volcaniclastic turbidites interbedded with submarine volcanic rocks (Adamia et al., 1977, 1981, 2011; Okrostsvaridze et al., 2018). From the Late Eocene until the Sarmatian, epiclastic sedimentation was largely predominant, with an overall shallowing upward trend (Adamia et al., 2011, 2017; Gamkrelidze et al., 2019).

The Adjara-Trialeti basin, after a post-rift stage of about 20 Ma, was structurally inverted starting at ca. 14 Ma (Middle Miocene) (Gusmeo et al., 2021, 2022; this paper). The ATFTB was then progressively incorporated in the advancing *retro*-wedge of the Lesser Caucasus during Neogene shortening of the area (Alania et al., 2021). In the early Late Miocene the marine connection between the Caspian and Black seas closed as a result of the continued convergence of the facing structural fronts of the south-verging GC and north-verging *retro*-wedge of the Lesser Caucasus orogenic prism (Banks et al., 1997; Nemčok et al., 2013; Alania et al., 2021; Gusmeo et al., 2021; Tari et al., 2021).

At the surface, Adjara-Trialeti inversion structures include broad anticlines and synclines bounded by high-angle reverse faults whereas low-angle thrust faults are common along the northern boundary of the ATFTB at the contact with the Kartli-Kura foreland basin. As to the subsurface, seismic data are characterized by mostly north-verging and subordinately south-verging duplex systems made of Cretaceous-Paleogene rocks, which accommodate variable amount of shortening (cf. Alania et al., 2021; Tari et al., 2021). Based on geodetic measurements, the ATFTB currently absorbs 3–6 mm/yr of the convergence rate between the eastern Anatolian Plateau and Eurasia (Reilinger et al., 2006; Sokhadze et al., 2018). Total shortening along the northern frontal structures was estimated at ~ 15 km (Bazhenov and Burtman, 2002); northward advancement of these frontal structures has progressively deformed the southern margins of the Rioni-Kartli foreland basin (Alania et al., 2017; Banks et al., 1997; Nemčok et al., 2013).

The southern Caucasian region (i.e. the Greater and Lesser Caucasus and the intervening Rioni-Kura foreland basin) absorbs a significant amount (~15 %–20 %) of the strain associated with the Arabia-Eurasia collision (Reilinger et al., 2006). The GPS velocity field indicates an anticlockwise motion relative to stable Eurasia, with northward motion increasing from ~ 2 mm/yr in the Rioni Basin close to the Black Sea coast to 12 mm/yr in the Kura Basin close to the Caspian Sea coast (Forte et al., 2013; Reilinger et al., 2006). Most deformation in the Caucasian region is accommodated in the domain comprised between the Greater and the Lesser Caucasus (named Transcaucasus; Karakhanyan et al., 2013; Sokhadze et al., 2018).

3. Previous thermochronologic work on the Greater Caucasus

Low-temperature thermochronologic data currently available for the GC are summarized in Table 1 and Figs. 3 and 4. Published data are mostly from the western sector of the orogen, with little information from the central and eastern sectors. We define as western, central and eastern GC the portions of the orogen west of 44°E longitude, between 44° and 46°E, and east of 46°E, respectively. Following is a concise description of the existing thermochronologic datasets; their implications -including those derived from the new data presented in this paper- will be presented in the Discussion section.

Over the years Stephen J. Vincent and co-workers have applied fission-track analysis on apatite (AFT) and zircon (ZFT), as well as

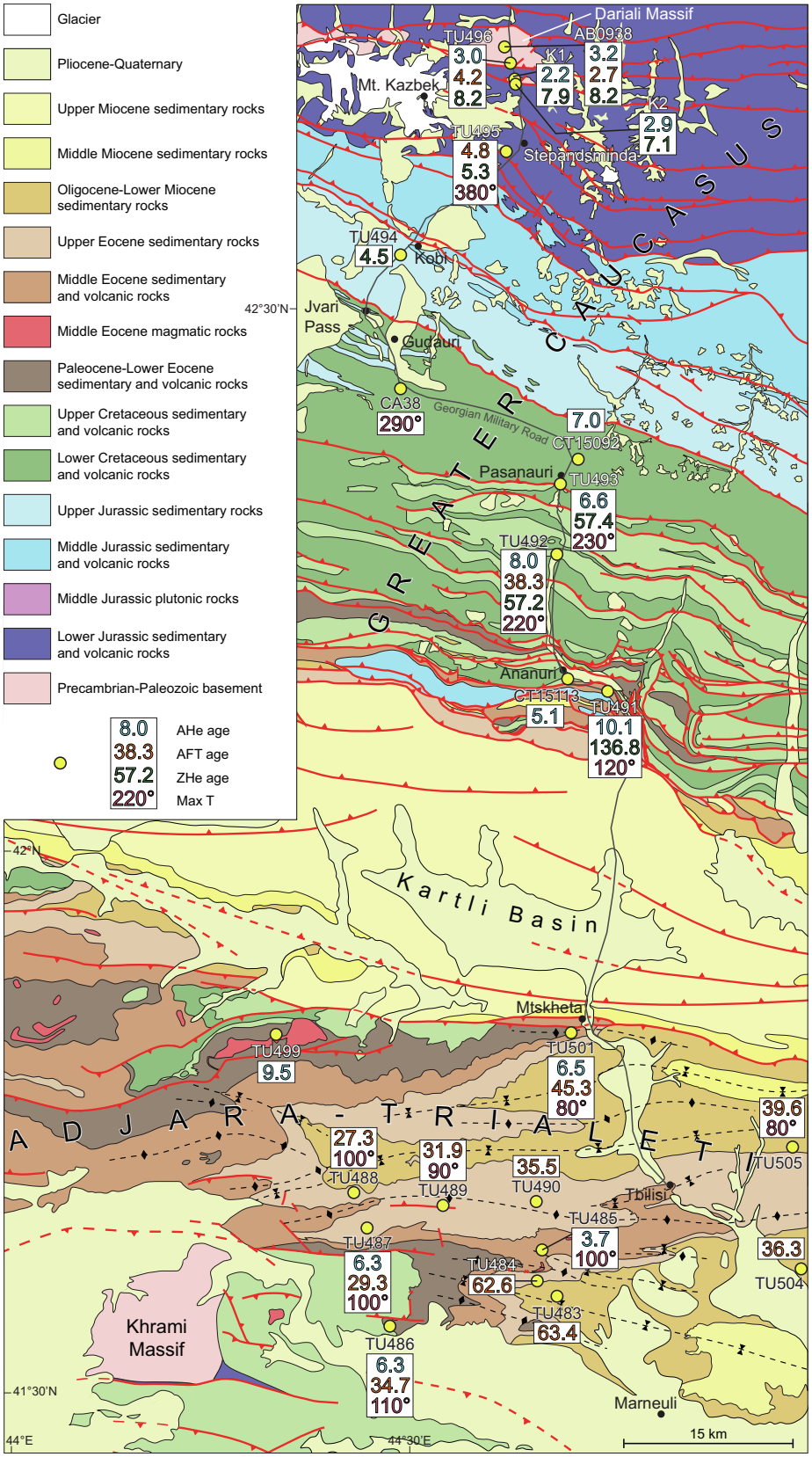

Fig. 2. Geological map of the study area across the southern central Greater Caucasus, the eastern Adjara-Trialeti fold-and-thrust belt and the Khrami Massif to the *retro*-wedge of the Lesser Caucasus (after Mosar et al., 2010, 2022; Tari et al., 2021), showing sample locations and results of low-temperature thermochronological analyses and maximum paleotemperature determinations. See Fig. 1 for location.

Table 1
Published thermochronologic datasets.

Domain	System	Age range (Ma)	N° samples	Reference
Western Greater Caucasus	AHe	25.4	1	Vincent et al., 2007
		25.4–49.5	3	Vincent et al., 2011
		1.7–19.0	10	Avdeev and Niemi, 2011
		5.6–24.5	5	Vincent et al., 2020
		3.3–6.2	3	Vasey et al., 2020
		1.9–4.2	3	Trexler et al., 2022
	AFT	1–68	44	Kral and Gurbanov, 1996
		57–176.4	9	Vincent et al., 2007
		2.5–264.2	27	Vincent et al., 2011
		3.6–21.8	6	Avdeev and Niemi, 2011
		1.4–48.2	19	Vincent et al., 2020
		4.6	1	Vasey et al., 2020
		4.2–136.6	4	Trexler et al., 2022
	ZHe	20.4–188.5	5	Avdeev and Niemi, 2011
		19.1–115.0	4	Vasey et al., 2020
	ZFT	139.6––271.5	4	Vincent et al., 2011
		230.4–433.0	3	Avdeev and Niemi, 2011
		1.7–231.6	4	Vincent et al., 2020
Central Greater Caucasus	AHe	5.1–7-0	2	Trexler et al., 2022
		2.2–3.2	3	Vasey et al., 2020
	AFT	2.7	1	Vasey et al., 2020
	ZHe	7.1–8.2	3	Vasey et al., 2020
Eastern Greater Caucasus	AHe	1.7–92.7	8	Avdeev, 2011
		3.1–4.9	6	Tye et al., 2022
	AFT	12.5–89.8	10	Bochud, 2018
		14–88.4	3	Avdeev, 2011
		6.1–15.5	5	Tye et al., 2022
	ZHe	10.8–91.8	2	Tye et al., 2022
	ZFT	102.8	1	Avdeev, 2011

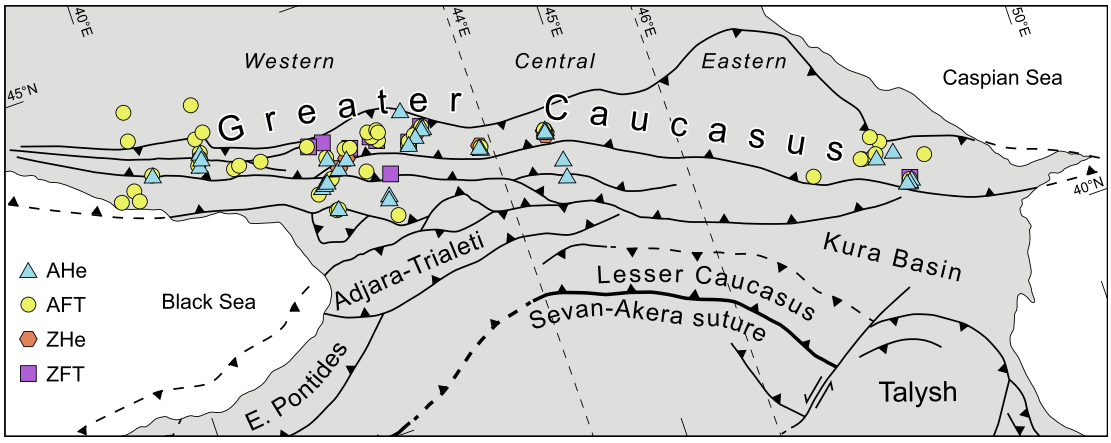

Fig. 3. Low-temperature thermochronologic data available for the Greater Caucasus distinguished by analytical method. See Table 1 for sources of data. Samples with ZHe/AHe single-grain age dispersion > 25 % or ZFT/AFT $P(\chi^2)$ < 5 have been omitted. Likewise, analyses not providing all the analytical details necessary for an independent assessment of the robustness of the data are not included.

(U-Th)/He analysis on apatite (AHe) on both rock and detrital (stream) samples from a wide area in the western GC. Earlier work (Vincent at al., 2007), integrated with stratigraphic evidence and heavy-mineral analyses from the foreland basins, suggested an earliest Oligocene minimum age for the subaerial uplift of the range, with initial uplift starting as early as the Late Eocene. Later work (Vincent et al., 2011, 2020), based on a larger dataset mainly focused on the crystalline core of the western GC, indicated no more than ~ 5–7 km of Cenozoic exhumation, with low rates during Oligo-Miocene times followed by acceleration during Late Miocene-Pliocene times. A marked along-strike change in Cenozoic cooling rates, with average AFT central ages of 32.5 Ma to the west of Mt. Elbrus and 6.3 Ma to the east of it, fundamentally agrees with earlier AFT data by Kral and Gurbanov (1996). Vincent et al. (2020), noting that the GPS velocity field along the southern slope of the western GC does not show a variation of shortening rates on either side of Mt. Elbrus, concluded that tectonic shortening, uplift, and exhumation can be excluded as drivers of the observed lateral variations in cooling rates and proposed thermally induced, mantle-driven dynamic uplift as the cause for differential exhumation. The region of rapid young cooling in the GC (Fig. 4) coincides with the area of recent magmatism and thermochronologic modes are consistent with buoyancy effects associated with mantle upwelling (Vincent et al., 2020; Bewick et al., 2022).

Avdeev and Niemi (2011) published fission-track and (U-Th)/He data on apatites and zircons from basement samples collected between Mt. Elbrus and Mt. Kazbek (42°50′ to 43°50′ longitude E). AFT central ages typically range between 8 and 5 Ma, in agreement with previous data on the same area (Kral and Gurbanov, 1996). ZHe and ZFT ages are mostly unreset, implying that the

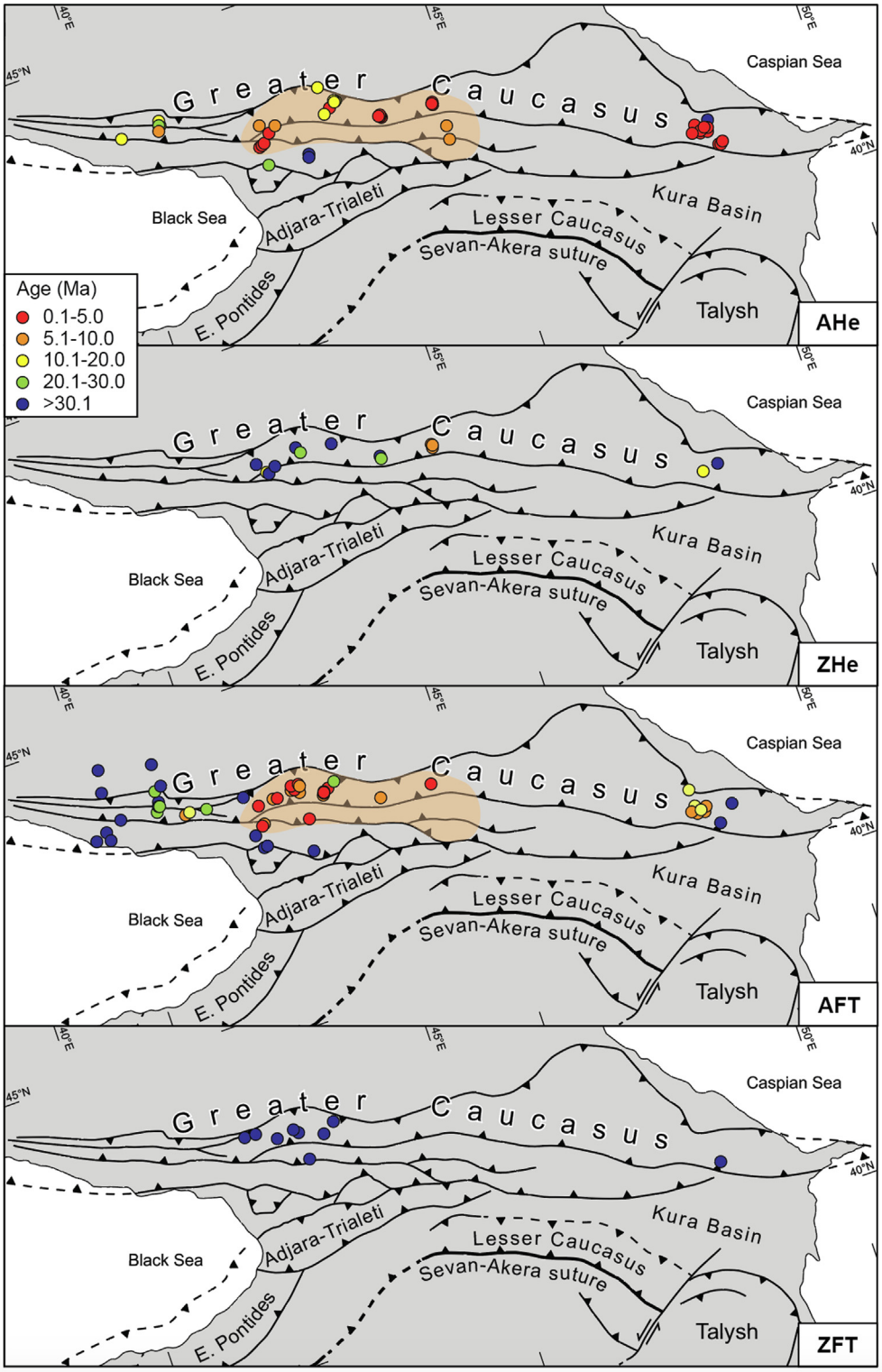

Fig. 4. Low-temperature thermochronologic data available for the Greater Caucasus distinguished by age. See Table 1 for sources of data. Samples with ZHe/AHe single-grain age dispersion > 25 % or ZFT/AFT $P(\chi^2)$ < 5 have been omitted. Likewise, analyses not providing all the analytical details necessary for an independent assessment of the robustness of the data are not included.

overall amount of Cenozoic exhumation in this region is less than 5–7 km. AHe results are rather dispersed, with single grain ages ranging between 22.9 and 0.7 Ma and a majority being younger than 5 Ma. Statistical modeling of integrated thermochronologic data show a marked increase of cooling rates at about 5 Ma (ca. Miocene-Pliocene boundary). Combining their data with those of Vincent et al. (2011), Avdeev and Niemi (2011) concluded that both the western and western-central portions of the GC experienced a Paleogene phase of slow exhumation whereas increased Plio-Pleistocene exhumation focused on the western-central portion. Such last period of exhumation is interpreted to represent the final closure of the GC basin and the collision between the

Lesser and Greater Caucasus, linked to the coeval reorganization of the Arabia-Eurasia collision zone (Allen et al., 2004). Such interpretation was shared by Cowgill et al. (2016), who envisioned a large GC basin which remained open until about 5 Ma, an interpretation which was the matter of some debate (see discussion and reply: Vincent et al., 2018; Cowgill et al., 2018).

Vasey et al. (2020) provide low-temperature thermochronologic data along two broadly N-S-oriented traverses in the western and central GC between about 42°20′ and 44°40′ longitude east. Two samples from the Dariali Massif, the easternmost outcrop of the Greater Caucasus basement, yielded ZHe mean ages between 7.9 and 7.1, and AHe mean ages comprised between 2.9 and 2.2 Ma (Table 1). These figures agree with unpublished data from another basement sample further to the north along the same transect (Avdeev, 2011). The authors use their thermochronologic dataset, together with other geochronologic and microstructural data, to conclude that the basement of the GC in the study area experienced at least ~ 5–8 km of rapid exhumation since about 10 Ma. The results from the Dariali Massif are relevant for this study and are discussed in more detail below.

More recently, Trexler et al. (2022) provided four AFT and three AHe ages from the western GC at a longitude of ~ 42°20′E, and two AHe results along a traverse in the central GC at ~ 44°40′E. Western samples yielded AFT central ages of 5.5 and 4.2 Ma to the north, and 136.6 and 104 Ma to the south. AHe mean ages are comprised between about 4.2 and 1.9 Ma. The central GC samples yielded AHe mean ages of 7.0 and 5.1 Ma.

Low-temperature thermochronologic data are unavailable over a long stretch of the GC between 45° and 47° longitude east (Fig. 3), an area of difficult access. More to the east, Avdeev (2011) reports one ZHe mean age (102.8 Ma), three AFT central ages ranging between 88.4 and 14.0 Ma, and eight AHe mean ages ranging between 4.0 and 1.7 Ma, with one outlier at 92.7 Ma. The author does not report the $P(\chi^2)$ for their AFT results nor the analytical details of (U-Th)/H analyses. Bochud (2011) provides ten AFT ages from Middle Jurassic and Neogene siliciclastic samples taken from 47°20′ to 48°10′ of longitude east. Central ages range between 89.8 and 12.5 Ma. The interpretation of this dataset is difficult as nine samples have a $P(\chi^2) < 5$ % thus pointing to the existence of multiple apatite grain populations. The only sample with $P(\chi^2) > 5$ % yielded a central age of 12.5 ± 2.4 Ma. Tye et al. (2022) have studied in detail the structural and thermochronologic evolution of distinct sedimentary rock packages within the eastern GC. They concluded that eastern GC exhumation started during Middle to Late Miocene time in the core of the orogen, where shale is abundant and distributed shortening was accommodated by pervasive folding. Accretion of a rheologically more competent rock package, the Vandam Zone, occurred between ca. 13 and 3 Ma and was followed by rapid exhumation (~0.3–1 mm/yr) starting between ca. 6 and 3 Ma.

4. Analytical methods and sampling

Standard rock crushing, density, and magnetic separation techniques were used to separate apatite and zircon grains from rock samples (Kohn et al., 2019). Mineral separations were performed at the Sedimentary Petrography Laboratory of the Department of Biological, Geological and Environmental Sciences, University of Bologna (Italy). We refer to Gusmeo et al. (2021) for a concise description of the fission-track and (U-Th)/He analytical methods and to Malusà and Fitzgerald (2019) for a thorough account. Descriptions of organic petrography (vitrinite reflectance), Raman spectroscopy on dispersed organic matter, Rock-Eval pyrolysis, and XRD clay mineralogy analyses can be found in Corrado et al. (2021) and Gusmeo et al. (2022). Details on sample preparation for all analytical methods can be found in Supplementary data.

As mentioned earlier, the published thermochronologic dataset for the central GC is fragmentary: just nine samples are available along an E-W stretch > 150 km long (Table 1). A single time–temperature inverse model is available for an area in excess of 15,000 km^3 (Vasey et al., 2020). Rather than adding other widely dispersed data points, we decided to focus our effort on what is arguably the better-known geological cross-section of the entire GC, the Georgian Military Road. The portion of this section in Georgian territory has been described in great detail in recent structural work (Mosar et al., 2022; Trexler et al., 2022), thus representing the best opportunity to tie thermochronologic data to a well-defined structural framework.

The studied samples were taken along a transect which cuts across the Jurassic-Oligocene sedimentary fill of the GC back-arc basin, now deformed into a stack of south-verging thrust sheets (Mosar et al., 2022; Trexler, 2022) (Figs. 1, 2). It then continues southward across the Kartli foreland basin and the eastern ATFTB. The samples analyzed are Variscan metamorphic rocks from the easternmost outcrop of the GC basement, the Dariali Massif, and Jurassic-to-Eocene detrital rocks representing the sedimentary fill of the GC basin (Fig. 2), which experienced considerable heating during burial (up to about 380 °C, under anchizone-epizone conditions; Corrado et al., 2021). In addition to the new results from the southern central GC, new low-temperature thermochronological results obtained from the eastern Adjara-Trialeti FTB and the Khrami Massif will be presented, providing further constraints on their tectonic evolution.

The apatite (U-Th)/He (AHe) dataset is composed of 59 single apatite grain aliquots (Fig. 2; Table 3) including 43 new analyses. The zircon (U-Th)/He (ZHe) dataset is composed of 27 single zircon grain aliquots (Fig. 2; Table 4) including 18 new analyses. The apatite fission-track (AFT) dataset comprises 24 samples (Fig. 2; Table 2) including 8 new samples.

Quantitative evaluation of the thermal histories of samples was carried out through inverse statistical modeling, which finds a range of cooling paths compatible with the available data (Ketcham 2005). In this work, inverse modeling of thermochronologic data was performed using the HeFTy program (Ehlers et al., 2005), which generates the possible *T*–*t* paths by means of a Monte Carlo algorithm. Predicted AFT data were calculated according to the Ketcham et al. (2007) annealing model for fission tracks revealed by etching. D_{par} values (i.e. the etch pit length) were used to define the annealing kinetic parameters of the grains and the original track length. Inverse modeling was based on the application of multiple thermochronometric techniques (AFT, AHe, ZHe) on the same samples and included also maximum burial temperatures obtained from vitrinite reflectance, clay mineralogy, and Raman spectroscopy (Corrado et al., 2021; Gusmeo et al., 2022), together with all other published geological constraints (intrusion ages, depositional ages, and stratigraphic relationships), to produce robust time–temperature evolutionary paths (Fig. 6). All constraints and parameters employed for the statistical modeling of each sample are listed in Supplementary data.

5. Analytical results

All thermochronometric data available for the study area are shown in Fig. 2 and listed in Tables 2-4. Analytical results are presented and discussed here from north to south. In the northernmost sector of the analyzed transect, the Dariali Massif is made of gneissic rocks metamorphosed at 330–310 Ma during the Variscan orogeny (Vasey et al., 2020). Samples from the Dariali Massif yielded ZHe mean ages of ~ 8–7 Ma (Fig. 2), with single-grain ages comprised between about 10 and 6 Ma (Table 4). The same samples yielded AHe mean ages around 3–2 Ma, with single-grain ages

Table 2
Results of apatite fission-track analyses.

Sample	Rock type	Age	Location	Elevation (m)	UTM coordinates (38 T)	No. crystals	Spontaneous		Induced		$P(\chi^2)$	Dosimeter		Age (Ma) ± 1sd	MCTL (μm) ± standard error	Standard deviation	No. tracks measured	D-par
							ρ_s	N_s	ρ_i	N_i		ρ_d	N_d					
AB0938[a]	Orthogneiss	Late Paleozoic	Greater Caucasus	1300	0469790 4731455	–	–	–	–	–	–	–	–	2.7 ± 0.4	–	–	–	–
TU483	Sandstone	Late Oligocene	Eastern ATFTB	684	0473006 4604652	42	0.18	222	0.71	871	94.18	14.50	7498	63.4 ± 5.8	14.10 ± 0.22	1.59	50	2.91
TU484	Granitoid clasts	Middle Jurassic	Eastern ATFTB	754	0472044 4605562	20	0.25	90	1.21	426	2.89	12.29	7683	62.6 ± 6.3	–	–	–	–
TU486[b]	Sandstone	Late Paleocene-Early Eocene	Eastern ATFTB	883	0456357 4599540	49	0.14	290	0.81	1691	99.68	12.22	7638	34.7 ± 2.8	12.05 ± 0.22	1.66	53	2.38
TU487[b]	Sandstone	Late Eocene	Eastern ATFTB	932	0452684 4611098	38	0.10	107	0.69	725	99.56	12.15	7593	29.3 ± 3.4	–	–	–	2.51
TU488[b]	Sandstone	Late Oligocene	Eastern ATFTB	1391	0452009 4616299	41	0.14	192	1.05	1393	99.44	12.07	7547	27.3 ± 2.5	12.48 ± 0.31	2.26	53	2.36
TU489[b]	Sandstone	Late Eocene	Eastern ATFTB	1291	0461429 4612640	13	0.09	36	0.53	224	97.20	12.00	7502	31.9 ± 5.9	–	–	–	2.35
TU490[b]	Sandstone	Late Eocene	Eastern ATFTB	1322	0472584 4613551	18	0.14	55	0.58	231	99.97	9.73	5046	35.5 ± 5.6	–	–	–	2.46
TU492	Sandstone	Cenomanian	Greater Caucasus	922	0473963 4680238	29	0.12	75	0.61	371	86.52	11.93	7457	38.3 ± 5.0	13.45 ± 0.20	1.54	62	2.86
TU495	Sandstone	Toarcian-Aalenian	Greater Caucasus	1754	0469216 4720975	24	0.67	41	27.97	1696	100.00	11.86	7411	4.8 ± 0.8	15.04 ± 0.13	1.20	85	2.61
TU496	Gneiss	Late Paleozoic	Greater Caucasus	1320	0469676 4730334	20	0.61	39	24.26	1563	100.00	9.65	5010	4.2 ± 0.7	15.19 ± 0.10	0.92	97	2.13
TU501[b]	Sandstone	Middle Eocene	Eastern ATFTB	561	0476497 4631400	88	0.16	574	0.64	2320	99.35	11.78	7366	45.3 ± 3.1	–	–	–	2.68
TU504[c]	Sandstone	Early Miocene	Eastern ATFTB	396	0500933 4602375	61	0.15	333	0.81	1770	99.98	11.64	7276	36.3 ± 2.8	13.34 ± 0.17	1.57	83	2.75
TU505[c]	Sandstone	Middle-Late Oligocene	Eastern ATFTB	512	0500906 4615010	48	0.24	270	1.17	1307	97.99	11.57	7230	39.63 ± 3.3	13.41 ± 0.18	1.47	67	2.31

ρ_s—spontaneous track densities ($\times 10^5$ cm^{-2}) measured in internal mineral surfaces; N_s—total number of spontaneous tracks; ρ_i and ρ_d—induced and dosimeter track densities ($\times 10^6$ cm^{-2}) on external mica detectors (g = 0.5); N_i and N_d—total numbers of tracks; $P(\chi^2)$—probability of obtaining χ^2 value for n degrees of freedom (where n = number of crystals −1); a probability > 5 % is indicative of a homogeneous population. Samples with a probability < 5 % were analyzed with the binomial peak-fitting method; MCTL—mean confined track length; a—Vasey et al. (2020); b—Gusmeo et al. (2021); c—Gusmeo et al. (2022).

Table 3
Results of (U-Th)/He analyses on apatites.

Sample	Rock type	Age	Location	Elevation (m)	UTM coordinates (38 T)	Replicate	Ft	Corrected age (Ma)	Error (Ma)	Mean age (Ma)	1sd error (Ma)	^{4}He (mol)	^{238}U (ppm)	^{235}U (ppm)	^{232}Th (ppm)	^{147}Sm (ppm)	eU	Rs (μm)
AB0938[a]	Orthogneiss	Late Paleozoic	Greater Caucasus	1300	0469790 4731455	AB0938b	–	3.50	0.04	3.2	0.5	–	41.0		46.9	296.7	–	56.1
						AB0938c	–	2.01	0.02			–	36.6		30.2	271.3	–	66.3
						AB0938d	–	3.42	0.03			–	23.8		43.1	361.0	–	42.9
						AB0938e	–	2.73	0.03			–	49.6		56.0	321.7	–	80.7
						AB0938f	–	2.27	0.03			–	32.2		31.5	230.7	–	52.0
						AB0938g	–	5.09	0.05			–	32.7		24.5	217.1	–	62.2
CT15092[b]	Sandstone	Early Cretaceous	Greater Caucasus	1130	0475989 4689034	–	–	–	–	7.0	0.1	–	–	–	–	–	–	–
CT15113[b]	Conglomerate	Early Cretaceous	Greater Caucasus	850	0475379 4667692	–	–	–	–	5.1	0.8	–	–	–	–	–	–	–
K1[a]	Granodiorite	Late Paleozoic	Greater Caucasus	1434	0469520 4728642	V16046Db	–	1.96	0.03	2.2	0.1	–	33.4		50.0	350.1	–	40.4
						V16046Dc	–	1.98	0.03			–	21.7		23.5	198.0	–	47.9
						V16046Dd	–	2.51	0.04			–	15.7		22.3	175.8	–	55.4
						V16046De	–	2.18	0.02			–	64.4		94.0	578.3	–	48.6
K2[a]	Mylonitic gneiss	Late Paleozoic	Greater Caucasus	1522	0469793 4728308	V16052Bc	–	3.35	0.05	2.9	0.3	–	10.8		20.6	141.9	–	56.3
						V16052Be	–	3.53	0.05			–	14.3		28.2	212.9	–	44.0
						V16052Bg	–	2.38	0.03			–	17.9		39.4	250.9	–	45.7
						V16052Bh	–	2.20	0.03			–	24.5		54.1	309.9	–	46.4
TU485[c]	Sandstone	Early Eocene	Eastern ATFTB	889	0472357 4609370	TU485-1	0.66	5.37	0.05	3.7	0.02	8.47*10^{-15}	8.68	0.07	69.94	39.25	25.12	44.75
						TU485-2	0.64	3.58	0.04			6.59*10^{-15}	19.87	0.16	81.87	35.89	39.11	42.75
						TU485-3	0.62	2.58	0.03			7.95*10^{-15}	33.50	0.27	288.22	81.36	101.24	38.51
						TU485-4	0.65	8.24	0.09			1.05*10^{-14}	14.72	0.12	50.43	15.33	26.58	42.55
						TU485-5	0.65	7.26	0.08			7.21*10^{-15}	9.38	0.09	61.75	43.71	23.90	46.95
TU486[c]	Sandstone	latest Paleocene-Early Eocene	Eastern ATFTB	883	0456357 4599540	TU486-1	0.66	5.93	0.18	6.1	0.1	4.96*10^{-15}	10.16	0.09	23.87	24.08	15.77	46.88
						TU486-3	0.73	17.32	0.16			4.69*10^{-14}	10.10	0.08	24.19	10.84	15.78	55.53
						TU486-4	0.68	13.62	0.20			1.58*10^{-14}	10.16	0.09	40.19	19.82	19.60	47.58
						TU486-5	0.66	4.08	0.06			4.55*10^{-15}	10.62	0.09	65.57	43.20	26.03	41.83
TU487[c]	Sandstone	Late Eocene	Eastern ATFTB	932	0452684 4611098	TU487-1	0.62	10.81	0.63	6.4	0.1	4.53*10^{-15}	6.91	0.08	39.88	29.50	16.28	38.85
						TU487-2	0.66	5.80	0.06			1.05*10^{-14}	17.46	0.14	79.57	75.61	36.16	45.53
						TU487-3	0.59	7.31	0.18			2.67*10^{-15}	9.20	0.10	37.49	16.87	18.01	36.91
						TU487-4	0.59	5.10	0.13			3.13*10^{-15}	16.15	0.15	64.32	54.55	31.27	35.21
						TU487-5	0.68	8.41	0.10			1.33*10^{-14}	16.19	0.13	54.02	42.30	28.88	96.94
TU491	Granitoid clasts in conglomerate	Late Eocene (conglomerate)	Greater Caucasus	772	0479248 4666600	TU491-1	0.69	13.66	0.23	10.1	3.4	5.50*10^{-15}	37.08		140.68	718.09	73.38	39.87
						TU491-2	0.73	9.72	0.17			8.94*10^{-15}	85.54		133.10	673.11	119.85	46.19
						TU491-3	0.65	6.97	0.31			9.96*10^{-16}	21.99		62.51	449.09	38.73	35.24
TU492	Sandstone	Cenomanian	Greater Caucasus	922	0473963 4680238	TU492_1	0.68	7.58	0.78	8.0	1.1	3.44*10^{-16}	5.23		25.13	198.65	12.04	38.96
						TU492_2	0.75	7.23	0.36			9.98*10^{-16}	6.16		35.42	189.89	15.34	51.52
						TU492_3	0.61	9.22	0.53			4.75*10^{-16}	13.19		86.17	353.23	35.02	30.83
TU493	Sandstone	Aptian-Albian	Greater Caucasus	1057	0474870 4688016	TU493-2	0.70	6.47	0.17	6.6	1.8	0.55*10^{-15}	18.71		17.75	123.09	22.88	42.18
						TU493-3	0.71	9.02	0.18			0.72*10^{-15}	13.90		33.53	101.85	21.78	42.63
						TU493-4	0.71	6.38	0.18			0.44*10^{-15}	28.46		6.66	116.43	30.02	43.34
						TU493-5	0.70	4.66	0.10			0.59*10^{-15}	33.75		66.92	401.64	49.47	42.05
TU496	Gneiss	Late Paleozoic	Greater Caucasus	1320	0469676 4730334	TU496-2	0.71	3.19	0.06	3.0	0.9	1.16*10^{-15}	44.30		53.39	295.89	56.85	42.93
						TU496-3	0.75	4.05	0.07			0.74*10^{-15}	20.51		27.70	201.34	27.02	50.20
						TU496-4	0.76	2.87	0.05			0.56*10^{-15}	23.20		24.83	198.45	29.04	53.60
						TU496-5	0.78	1.82	0.02			1.40*10^{-15}	67.49		134.62	442.35	99.12	58.43
TU499[c]	Sandstone	Early Eocene	Eastern ATFTB	1338	0445544 4631754	TU499-2	0.62	8.85	0.24	9.5	0.9	1.02*10^{-15}	3.46	0.10	20.17	1.87	8.20	37.87
						TU499-3	0.55	10.18	0.24			1.34*10^{-15}	6.77	0.15	40.35	11.07	16.25	32.19
TU501[c]	Sandstone	Middle Eocene	Eastern ATFTB	561	0476497 4631400	TU501-1	0.71	5.89	0.06	6.5	0.04	1.13*10^{-14}	11.67	0.09	44.51	44.45	22.13	53.27
						TU501-2	0.62	9.95	0.16			5.81*10^{-15}	8.63	0.08	40.63	29.07	18.17	39.50
						TU501-3	0.67	8.74	0.10			1.24*10^{-14}	12.88	0.11	68.94	27.90	29.08	44.97
						TU501-4	0.60	6.86	0.20			2.08*10^{-15}	7.30	0.09	34.11	26.01	15.32	37.75
						TU501-5	0.61	5.46	0.07			3.26*10^{-15}	11.41	0.11	58.72	32.88	25.21	38.48

The effective uranium value (eU = [U] + 0.235*[Th]) gives an indication of the goodness of the data: if < 5 the uranium content of the apatite crystal is too low to provide a meaningful result. All replicates considered in the discussion have eU > 5; Rs—equivalent radius; a—Vasey et al. (2020); b—Trexler et al. (2022); c—Gusmeo et al. (2021).

Table 4
Results of (U-Th)/He analyses on zircons.

Sample	Rock type	Age	Location	Elevation (m)	UTM coordinates (38 T)	Replicates	Ft	Corrected age (Ma)	Error (Ma)	Mean age (Ma)	1sd error (Ma)	^{4}He (mol)	^{238}U (ppm)	^{232}Th (ppm)	eU	Rs (μm)
AB0938[a]	Orthogneiss	Late Paleozoic	Greater Caucasus	1300	0469790 4731455	AB0938Zra	0.77	7.43	0.08	8.2	1.0	–	2746.5	659.6	2901.5	48.8
						AB0938Zrb	0.76	6.88	0.07			–	1701.3	748.2	1877.1	46.6
						AB0938Zrc	0.75	10.24	0.10			–	1912.6	591.8	2051.7	44.2
K1[a]	Granodiorite	Late Paleozoic	Greater Caucasus	1434	0469520 4728642	V16046DZra	0.74	7.44	0.08	7.9	0.3	–	1048.1	334.1	1126.6	45.3
						V16046DZrb	0.73	8.30	0.09			–	479.4	163.5	517.8	42.0
						V16046DZrc	0.77	8.00	0.08			–	1135.7	362.1	1220.8	49.5
K2[a]	Mylonitic gneiss	Late Paleozoic	Greater Caucasus	1522	0469793 4728308	V16052BZra	0.75	5.86	0.06	7.1	0.7	–	1087.4	355.4	1170.9	44.8
						V16052BZrb	0.71	8.10	0.08			–	1159.7	503.8	1278.1	41.1
						V16052BZrc	0.73	7.28	0.08			–	1143.1	409.3	1239.3	42.0
TU491	Granitoid clasts	Late Eocene (conglomerate)	Greater Caucasus	772	0479248 4666600	TU491-1	0.84	135.71	1.82	136.8	1.1	$1.44*10^{-12}$	297.2	231.0	351.5	68.0
						TU491-2	0.84	136.73	1.93			$1.25*10^{-12}$	264.6	142.0	298.0	71.6
						TU491-3	0.86	137.99	1.97			$1.70*10^{-12}$	252.9	115.9	280.1	78.2
TU492	Sandstone	Cenomanian	Greater Caucasus	922	0473963 4680238	TU492_2	0.75	57.21	0.76	57.2	0.8	$2.22*10^{-13}$	407.8	303.9	479.3	43.1
TU493	Sandstone	Aptian-Albian	Greater Caucasus	1057	0474870 4688016	TU493-3	0.72	57.42	0.79	57.4	0.8	$4.88*10^{-14}$	217.7	190.2	262.4	37.7
TU494	Sandstone	Oxfordian-Tithonian	Greater Caucasus	2021	0458552 4711144	TU494-1	0.70	5.31	0.08	4.5	0.7	$8.00*10^{-15}$	517.0	83.4	536.6	34.9
						TU494-2	0.69	3.95	0.06			$7.13*10^{-15}$	752.1	132.1	783.1	33.3
						TU494-3	0.66	4.32	0.06			$2.64*10^{-15}$	433.7	287.0	501.1	29.9
TU495	Sandstone	Toarcian-Aalenian	Greater Caucasus	1754	0469216 4720975	TU495-1	0.78	5.05	0.07	5.3	0.5	$4.70*10^{-14}$	675.4	226.9	728.8	49.6
						TU495-2	0.76	5.86	0.08			$2.08*10^{-14}$	397.7	254.3	457.5	44.6
						TU495-3	0.74	4.99	0.07			$1.59*10^{-14}$	491.6	296.8	561.3	41.1
TU496	Gneiss	Late Paleozoic	Greater Caucasus	1320	0469676 4730334	TU496-1	0.84	9.34	0.12	8.2	1.2	$5.82*10^{-13}$	1834.8	840.1	2032.2	70.3
						TU496-2	0.87	7.03	0.09			$6.88*10^{-13}$	1533.1	653.9	1686.7	83.2
						TU496-3	0.80	8.23	0.12			$1.18*10^{-13}$	926.7	152.6	962.6	53.7

eU—effective uranium value (eU = [U] + 0.235*[Th]); Rs—equivalent radius; a—Vasey et al. (2020).

comprised between about 5 and 2 Ma (Table 3), and two of them yielded AFT central ages around 4–3 Ma (Fig. 2; Table 2). The low dispersion of He ages and the very high $P(\chi^2)$ value of the AFT results indicate that the samples experienced rapid cooling across the closure temperature of the respective thermochronometric systems, thus pointing to very fast cooling from > 180 °C to < 40 °C during Late Miocene-Pliocene times (10–2 Ma).

South of the Dariali Massif, two Jurassic sandstone samples from the inverted GC basin-fill yielded ZHe single-grain ages comprised between about 6 and 4 Ma (Table 4), and one of them yielded an AFT central age of 4.8 ± 0.8 Ma (Fig. 2; Table 2). Thermal maturity analyses (Corrado et al., 2021) on the same samples (Raman spectroscopy, I% in I-S mixed layers and Kübler Index) indicate that they have experienced maximum temperatures > 300 °C (anchizone-epizone conditions). The results show that also this sector was exhumed quickly, coevally with the Dariali Massif.

Moving further south, three sandstone samples from the Early to early Late Cretaceous succession of the GC basin-fill yielded AHe single-grain ages comprised between about 9 and 5 Ma. Two of these samples yielded ZHe ages around 57 Ma and one of them yielded an AFT central age of 38.3 ± 5.0 Ma (Fig. 2; Tables 2-4). Thermal maturity analyses indicate that these samples experienced maximum burial temperatures > 200 °C (Corrado et al., 2021). The young AHe ages are coeval with those found more to the north along the transect. AFT and ZHe ages indicate that these samples cooled from more than ~ 180 °C to less than ~ 110 °C during Paleocene-Eocene times.

Two coarse grained sedimentary units were sampled in the GC foothills and analyzed. One of them (CT15113; Trexler et al., 2022) is a Lower Cretaceous conglomerate, and the other one (TU491; this study) is an Upper Eocene conglomerate. The Early Cretaceous conglomerate yielded an AHe age of ca. 5 Ma, whereas the Late Eocene conglomerate yielded a ZHe age of about 137 Ma and AHe single-grain ages between about 14 and 7 Ma (Fig. 2; Tables 3 and 4). Thermal maturity analyses on the sedimentary rocks in this sector indicate that they experienced maximum burial temperatures of 100–150 °C (Corrado et al., 2021), thus confirming that the AHe system is fully reset, as opposed to the ZHe system.

In the eastern ATFTB, new apatite fission-track results have been obtained from three Oligocene-Miocene sandstones (TU483, TU504, and TU505; Fig. 2; Table 2). All three samples have high $P(\chi^2)$ values, indicating a single population of grains, and yielded AFT central ages of 63.4, 36.3, and 39.6, respectively. Thermal maturity analyses on the same samples, or in nearby sedimentary rocks, show that these samples are partially or non-reset (Corrado et al., 2021).

In the following we focus on the results of statistical inverse models integrating all available data, thus avoiding the potential pitfalls of using only fission-track central ages (Jess et al., 2020) or (U-Th)/He mean ages which can be confounding "averages" of complex thermal histories (Malusà and Fitzgerald, 2019). Radial plots of single-grain apatite fission-track (AFT) ages and histograms showing the confined-track length distributions of apatite grains for the samples used for statistical inverse modeling are shown in Fig. 5. The eight models shown in Fig. 6 are robust as they integrate (i) multiple low-temperature thermochronometers as well as, where available, (ii) maximum burial temperatures obtained from organic matter and clay mineralogy thermal indicators (Corrado et al., 2021; Gusmeo et al., 2022) and (iii) all other published geological constraints (intrusion ages, depositional ages, and stratigraphic relationships).

Inverse models are remarkably coherent. Time-temperature paths derived from samples taken across the central GC (TU496, TU495, TU493, TU492) show a first phase of rapid cooling during the Late Cretaceous - Paleocene (green bars, Fig. 6). Cooling is slightly older in the core of the orogen and becomes younger towards its frontal part to the south, thus pointing to an overall southward progression of exhumation. A long interval of slow or no cooling occurred from the Eocene to the Early Miocene, followed by a second phase of rapid cooling starting in the mid-Miocene, with increased cooling rates from the Late Miocene (since about 10 Ma) to the present (orange bars, Fig. 6).

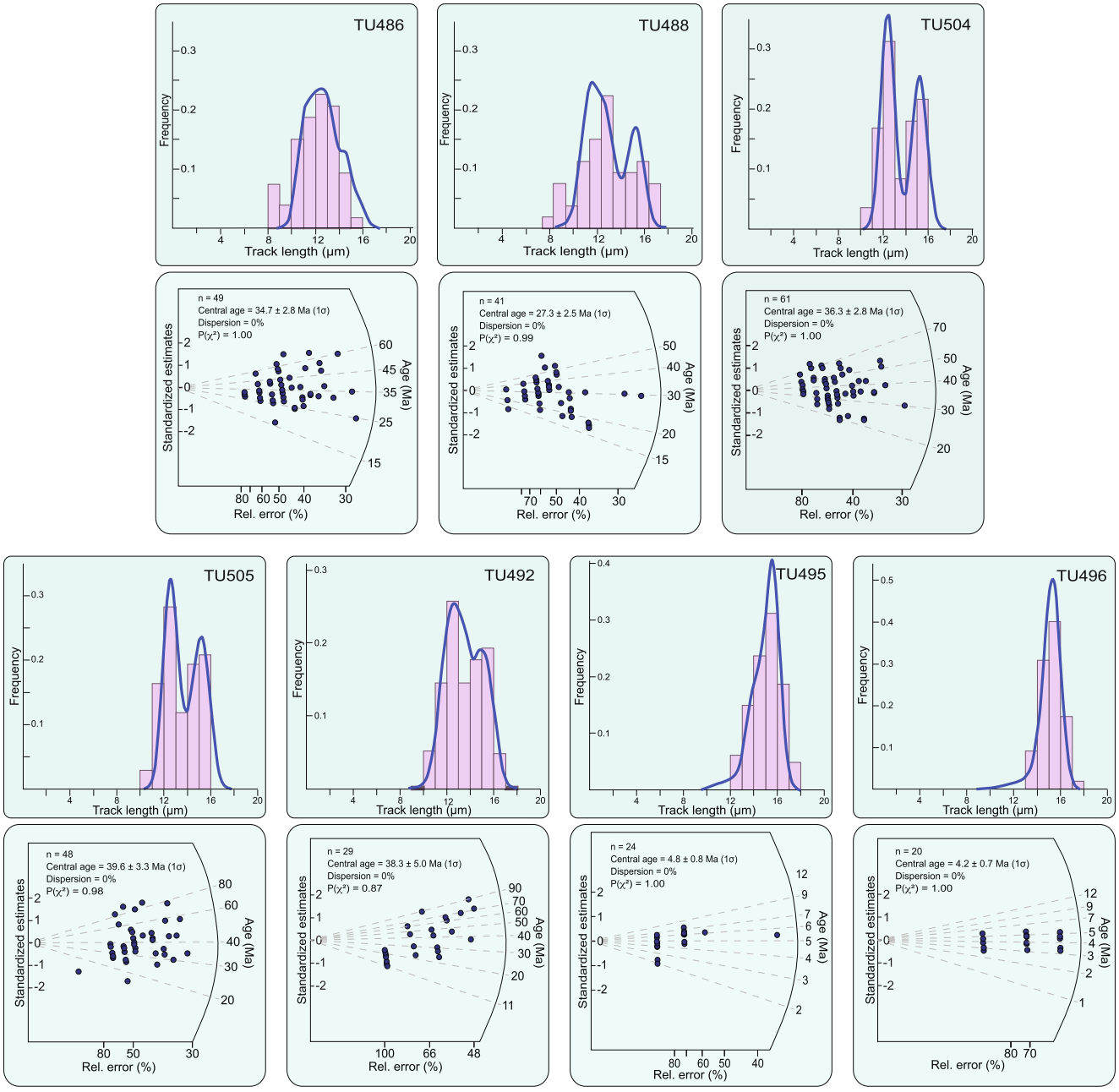

Fig. 5. Radial plots of single-grain apatite fission-track (AFT) ages and histograms showing the confined-track length distributions of apatite grains for the samples used for statistical inverse modeling. Samples are ordered as in Fig. 6.

The *t-T* paths derived from the AT inverted rift basin fill (505, 504, 488, 486) also show two discrete phases of cooling. The younger one occurred in the Miocene starting between 20 and 10 Ma (see also Corrado et al., 2021; Gusmeo et al., 2021, 2022). Plio-Quaternary cooling rates are slower, in contrast with the GC which has been exhuming rapidly over the last few million years (see also Forte et al., 2022). Sedimentary samples from AT are partially reset with reference to the apatite fission-track closure temperature and thus retain a partial memory of the cooling history of their sediment source-areas; their inverse models indicate that the analyzed apatite grains were eroded from a source area which experienced a phase of cooling/exhumation between ca. 60 and 40 Ma (green bars, Fig. 6).

6. Discussion

Joint inversion of our AFT, ZHe and AHe data from the Greater Caucasus and the Adjara-Trialeti fold-and-thrust belt, integrated with thermal maturity and stratigraphic data, resolves two discrete phases of intraplate cooling/exhumation (Fig. 6) which can be chronologically and spatially correlated to the development of the two suture zones characterizing the geology of Anatolia and the Caucasian region: the Sevan-Akera and Bitlis sutures. (i) The *Sevan-Akera suture* is the eastern continuation of the İzmir-Ankara-Erzincan suture zone (Fig. 1A), marking the closure of the northern Neotethys in Late Cretaceous - Paleocene times and the ensuing collision between the Anatolide-Tauride-Armenian ter-

rane of Gondwanan affinity and the southern Eurasian (Laurasian) continental margin (Okay and Tüysüz, 1999; Stampfli and Hochard, 2009; Sosson et al., 2010; Barrier et al., 2018) (Fig. 7B). It is the major suture in Anatolia and the Caucasian region as it extends from north of İzmir eastward to the border with Armenia from where it continues as the Sevan-Akera suture in the Lesser Caucasus (Khain, 1975; Knipper, 1980; Adamia et al., 1981; Sosson et al., 2010). To the west, the Izmir-Ankara-Erzincan suture links across the Aegean Sea to the Vardar suture in the Balkan peninsula. (ii) The *Bitlis suture*, separating the Anatolide-Tauride-Armenian terrane to the north from the Arabian plate to the south, resulted from the closure of the southern branch of the Neotethys (Yılmaz, 1993; Okay and Tüysüz, 1999; Stampfli and Hochard, 2009; Barrier et al., 2018) (Fig. 7D). The Bitlis suture continues to the south-east for over 1,500 km as the Zagros suture, marking the progression of an oblique and diachronous continental collision, with estimates ranging between 35 and 5 Ma (Late Oligocene - Miocene; e.g. Dewey et al., 1973; Bird et al., 1975; Allen and Armstrong, 2008; Mouthereau et al., 2012; McQuarrie and van Hinsbergen, 2013; Saura et al., 2015; Pirouz et al., 2017). Fast mid-Miocene cooling/exhumation along the Bitlis suture zone marked the beginning of head-on hard collision between Arabia and Eurasia in the region of maximum indentation (Okay et al., 2010; Cavazza et al., 2018).

The stress field of plate interiors comprises transitory components induced by geologically rapid changes at plate boundaries which may trigger actual intraplate deformation at suitable locations (see Stephenson et al., 2020, for a review). Our results show that the structural inversions of the GC and AT rift basins are prime examples of the existence and action of intraplate stresses originating from different sources at different times and causing cumulative, superposed effects on the same inherited geological structures. The argument for transmission of plate boundary stresses is supported by the matching tectonic evolution of the accretionary southern margin of the Eurasian plate. The GC is a growing intraplate orogen in a relatively young stage of its development (Forte et al., 2022); this still provides the opportunity to resolve earlier individual deformation pulses which in a more evolved orogen would be obfuscated by the cumulative effects of progressive deformation over longer time spans. The ATFTB is a mildly inverted rift basin which still retains the thermochronologic memory of cooling/exhumation episodes in the source area of its sedimentary basin fill. In the following two sections we elaborate on the timing, spatial distribution, and significance of the two cooling/exhumation episodes recorded by the analyzed samples, with focus on the results from the Greater Caucasus.

6.1. Latest Cretaceous-Paleocene cooling/exhumation

The thermochronologic evolution of the central GC basin fill and its basement invariably points to a stage of rapid cooling starting in the latest Cretaceous (Fig. 6), in agreement with the diachronous collision of the Anatolide-Tauride-Armenian terrane with Eurasia (latest Cretaceous - Paleocene) (Okay and Tüysüz, 1999; Stampfli and Hochard, 2009; Sosson et al., 2010) (Fig. 7B). Evidence of latest

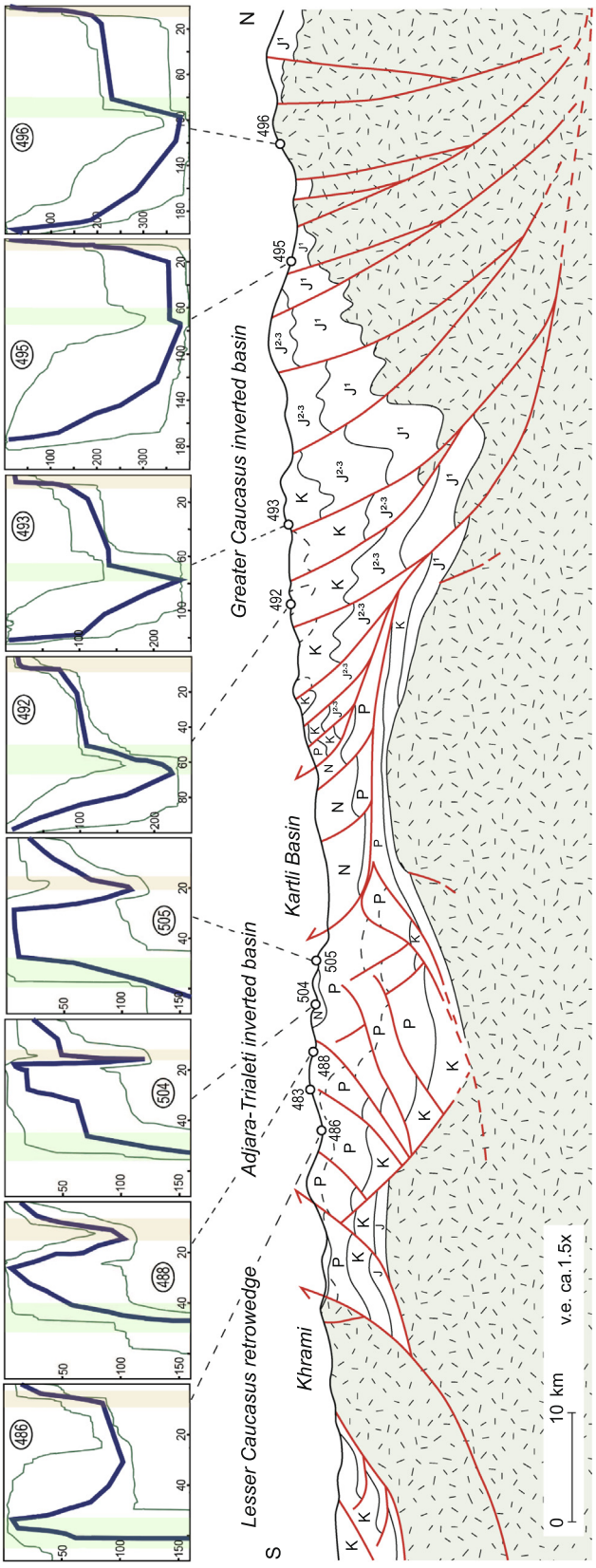

Fig. 6. Schematic structural cross-section from the southern pro-wedge of the central Greater Caucasus, across the western Kura Basin (also called Kartli Basin) and the eastern Adjara-Trialeti fold-and-thrust belt, to the northernmost tip of the Lesser Caucasus retro-wedge (after Nemčok et al., 2013; Tari et al., 2021; Mosar et al., 2022; our unpublished data). Statistical inverse modelling results of eight representative samples, projected along the profile, are shown, with time (Ma) on the x-axis and temperature (°C) on the y-axis. Envelopes include all t-T paths having a statistically robust goodness-of-fit (GOF > 0.5); blue lines indicate best-fit paths. Green and orange vertical stripes indicate two discrete cooling episodes in the latest Cretaceous - Paleocene and the late Neogene. V.E. = vertical exaggeration. (For interpretation of the references to colour in this figure legend, the reader is referred to the web version of this article.)

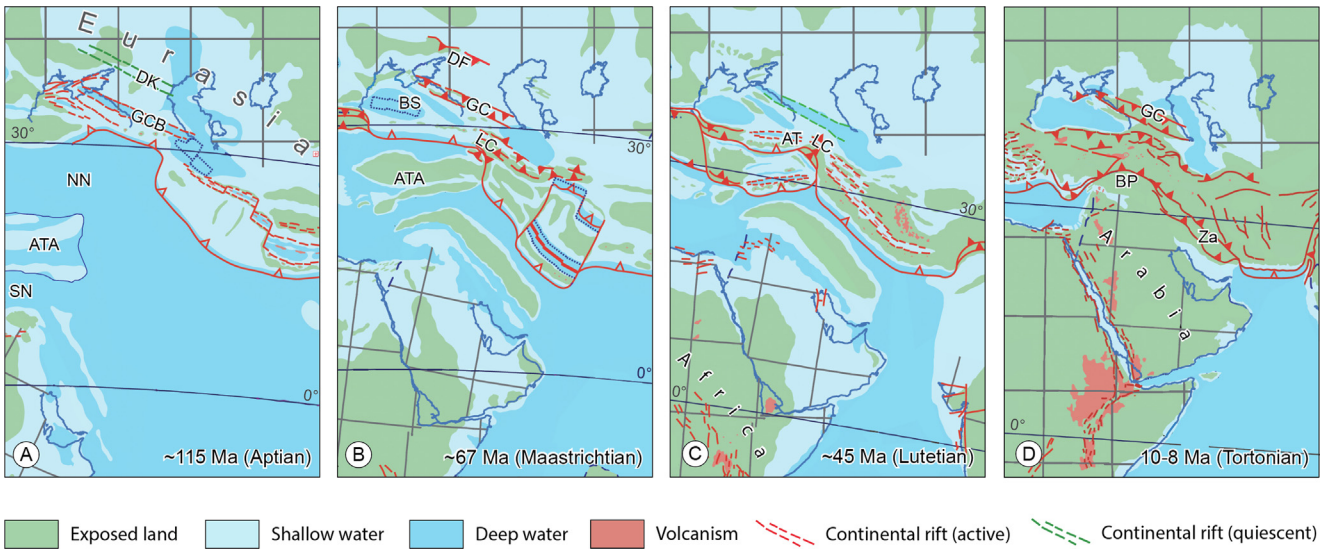

Fig. 7. Paleogeographic sketch maps showing the evolution of the Arabia-Eurasia convergence zone (after Barrier et al., 2018). Aptian: both the northern and southern branches of the Neotethys were open. Late Maastrichtian: continental collision between the Anatolide-Tauride-Armenian terrane and Eurasia was ongoing, forming the Lesser Caucasus orogenic wedge and causing partial inversion of the intraplate Greater Caucasus basin and mild deformation of the Donbas foldbelt. Middle Eocene: widespread extension in the upper (Eurasian) plate triggering the opening, among others, of the Adjara-Trialeti back-arc basin. Middle Miocene: Arabia-Eurasia hard collision along the Bitlis suture caused compressional deformation in a wide region of the hinterland, including structural inversion of the Adjara-Trialeti and Greater Caucasus back-arc basins. AT = Adjara-Trialeti back-arc basin; ATA = Anatolide-Tauride-Armenian terrane; BP = Bitlis-Pütürge Massif; BS = Black Sea; DF = Donbas foldbelt; DK = Donetsk-Donbas-Karpinsky rift; GC = Greater Caucasus orogen; GCB = Greater Caucasus Basin; LC = Lesser Caucasus; NN = Northern Neotethys; SN = Southern Neotethys; Za = Zagros fold-and-thrust belt.

Cretaceous - Paleocene deformation has been shown in other areas of the GC basin. For example, during this time interval (i) marginal basin-fill successions were thrust over the rift basin shoulders along the southern edge of the central GC (Candeaux, 2021), (ii) deformation greatly changed the geometry of the basin which was partitioned in a number of smaller depocenters (Blackbourn et al., 2021), and (iii) tectonic instability is recorded by a Paleocene unconformity (Mosar et al., 2022). A widespread Early Paleocene (ca. 64–60 Ma) unconformity also occurs to the south of the GC basin in the area which then became the Rioni foreland basin (Tari et al., 2018). Senonian-Paleocene intraplate compressional deformation and exhumation is widespread in the sector of the East European Platform directly to the north of the GC like, for example, in the Donbas foldbelt, the southeastern termination of the Middle-Late Paleozoic Pripyat-Dnieper-Donets rift basin (Stovba and Stephenson, 1999; Maystrenko et al., 2003; Saintot et al., 2003; Danišík et al., 2010; Kopp et al., 2010; Stephenson et al., 2001) (Fig. 7B).

Late Cretaceous shortening is well documented also in the Lesser Caucasus of Azerbaijan and Armenia (e.g. Barrier et al., 2018) (Fig. 7B), where its thermochronologic signature is still locally present despite widespread overprinting by Middle-Late Miocene shortening (Cavazza et al., 2019). The growing Lesser Caucasus orogen was an important sediment source for the AT basin sedimentary fill (Gusmeo et al., 2021) as also shown by thermochronologic inverse modeling of basin-fill samples (Fig. 6). Such samples, partially reset with respect to the AFT system, consistently indicate fast cooling/exhumation of the sediment source-area during the Paleocene-Early Eocene, a timing in agreement with orogenic growth of the Lesser Caucasus.

The results of apatite fission-track analysis and statistical inverse modeling from the Khrami Massif also point to inception of slow cooling/exhumation during Paleocene-Early Eocene times (Cavazza et al., 2019; Gusmeo et al., 2021), likely the result of continental collision along the Sevan-Akera suture. This interpretation is supported by industrial seismic lines which indicate that the massif is the surficial expression of a north-vergent basement thrust sheet, overlying a structural duplex made of Jurassic-Cretaceous rocks, within the retro-wedge of the Lesser Caucasus (Gusmeo et al., 2021).

6.2. Miocene cooling/exhumation

The new thermochronological dataset obtained across the central GC and the AT fold-and-thrust belt indicates fast cooling/exhumation since the Miocene. Strain sequences along a large and complex orogen such as the GC are characteristically diachronous and therefore the results of this study apply directly only to the central portion of the GC. Nonetheless, other thermochronological data obtained more to the west (Avdeev and Niemi, 2011; Vincent et al., 2011, 2020; Vasey et al., 2020) and to the east (Avdeev, 2011; Bochud, 2011; Tye et al., 2022) are broadly in agreement, suggesting that since the Middle Miocene fast uplift/exhumation affected a wide area.

Available fission-track central ages and (U-Th)/He mean ages are somewhat different along the strike of the GC (Fig. 4). Ages < 10 Ma are concentrated east of ~ 42° longitude E whereas to the west Late Miocene-to-present ages are virtually absent. For example, the average AFT age to the east of Mt. Elbrus is 6.3 Ma, whereas to the west is 32.5 Ma. Kral and Gurbanov (1996) proposed that the marked change in AFT ages that they recorded on either side of Mt Elbrus activity was due to a major NNE–SSW-trending basement fault, but no clear structures are apparent in the surface geology of the western Greater Caucasus that can be attributed to this feature nor there is evidence for seismicity along this trend (Vincent et al., 2011). Such longitudinal difference has fueled the hypothesis that the western and central GC underwent substantially different cooling histories, with an abrupt westward decrease in exhumation rate. These differences have been explained in terms of buoyancy effects related to the asthenospheric replacement of lithospheric mantle (Vincent et al., 2020). While it is true that the region with young cooling ages coincides with an area of mantle-sourced Late Miocene and younger magmatism, it should be also considered that statistically robust ther-

mochronologic inverse models available for the western and central GC at longitudes ranging between 40 and 44°E (Avdeev and Niemi, 2011, in this reference's Figs. 4, 7; Vincent et al., 2011, in this reference's Fig. 5, 2020, Fig. 9; Vasey et al., 2020, in this reference's Fig. 6) invariably show increased cooling starting from the Serravallian-Messinian (Middle-Late Miocene; ~14–5 Ma) and clear-cut longitudinal trends are absent. The discrepancy between single ages and integrated statistical models underscores an important issue which is often neglected in thermochronology studies: FT central ages and (U-Th)/He mean ages are hardly significant by themselves if the analyzed samples underwent a complex thermal history (Malusà and Fitzgerald, 2019; Jess et al., 2020). Such cases can be resolved by statistically integrating high-quality results of multiple thermochronologic analytical techniques. Unfortunately, the density of thermochronologic inverse models currently available is still too low to develop a meaningful cooling/exhumation pattern for the entire orogen, particularly for its eastern portion, but a picture of widespread Middle-Late Miocene cooling with some acceleration from ca. 5 Ma is emerging. Within this overall trend there might be finer distinctions (i.e. a general eastward younging trend) but they are not yet clearly established at this stage, particularly considering the intrinsic limitations of the dataset currently available.

Structural and stratigraphic data from the GC and the adjacent foreland basins indicate widespread orogenic growth since the Middle Miocene. For example, Sarmatian (late Middle-early Late Miocene) marine sediments are now found at elevations reaching 4,000 m in the eastern GC, indicating very fast uplift in the last ~ 10 Ma (Mosar et al., 2010). Inception of deformation in the Kura foreland fold-and-thrust belt, to the south of the central-eastern GC and resulting from its southward propagation, also started during Middle-Late Miocene times, as shown by growth strata geometries and thermal maturity data (Alania et al., 2017; Corrado et al., 2021; Gusmeo et al., 2022). Growth strata geometries in the Rioni foreland basin also indicate that south-directed deformation in response to the western GC uplift occurred since Middle Miocene times. In this basin, coarser clastics became predominant since the mid-Miocene, marking a clear-cut transition from the finer grained sedimentary deposits of the Maykop succession (Tari et al., 2018). On the northern side of the orogen, seismic lines interpretation, subsidence studies from boreholes data, and stratigraphic analyses all indicate important deformation/uplift in the GC since the Middle Miocene (e.g. Mosar et al., 2010; Sobornov, 2021).

The dataset by Vincent and coworkers (2007, 2011, 2020) has been interpreted in the subsequent literature to conclude that GC exhumation began around the Eocene-Oligocene boundary. In reality, the original interpretation is cautious: *"the thermochronometric data are not sufficiently detailed to be able to better constrain time–temperature pathways . . . of the range, other than to confirm general Oligo-Miocene cooling and identify a number of pulsed events during this evolution . . . The resolution of these events is not well constrained, although it would appear that cooling was most pronounced during the Miocene epoch"* (Vincent et al., 2011). Our thermochronometric inverse models (Fig. 6), in agreement with most of the few thermal histories available in the literature (Bochud, 2011; Vincent et al., 2011; Avdeev and Niemi, 2011; Vasey et al., 2020), contradict the traditional notion, much ingrained in the older literature, that GC uplift initiated in the Oligocene. Such supposed uplift was considered the result of the Arabia-Eurasia collision, an interpretation which is difficult to reconcile with the fact that during the Oligocene the AT rift basin, despite being located between the Bitlis suture and the GC basin, was still undeformed (Gusmeo et al., 2021). At least two other observations provide further support to a post-Oligocene uplift of the GC: (i) Oligocene depocenters in the Kura foreland basin are aligned along its southern margin (i.e. there was no GC-induced flexural subsidence during the Oligocene) (Nemčok et al., 2013); (ii) the Oligocene sediment paleodispersal system north of the GC is oriented southward, from the Scythian-Russian platform towards the GC (i.e. there was no significant erosion and sediment generation derived from the GC) (Sobornov, 2021).

Chronologically, the pulse of Miocene cooling/exhumation in the Caucasian domain at large fits the timing of Arabia-Eurasia hard collision (and hinterland deformation) and can be considered as a result of the northward transmission of far-field compressional stresses from the Bitlis suture (Okay et al., 2010; Cavazza et al., 2018). The elastic stresses propagating from the Arabia-Eurasia plate boundary were relaxed by compressional reactivation of pre-existing faults (Gusmeo et al., 2021; Mosar et al., 2022). Neogene intraplate deformation started earlier (mid-Miocene) in the AT backarc basin -situated closer the Bitlis collision zone- and kicked off in the central GC only later in the Late Miocene (Figs. 6, 7D), when compressional stresses were transmitted farther into the plate interior.

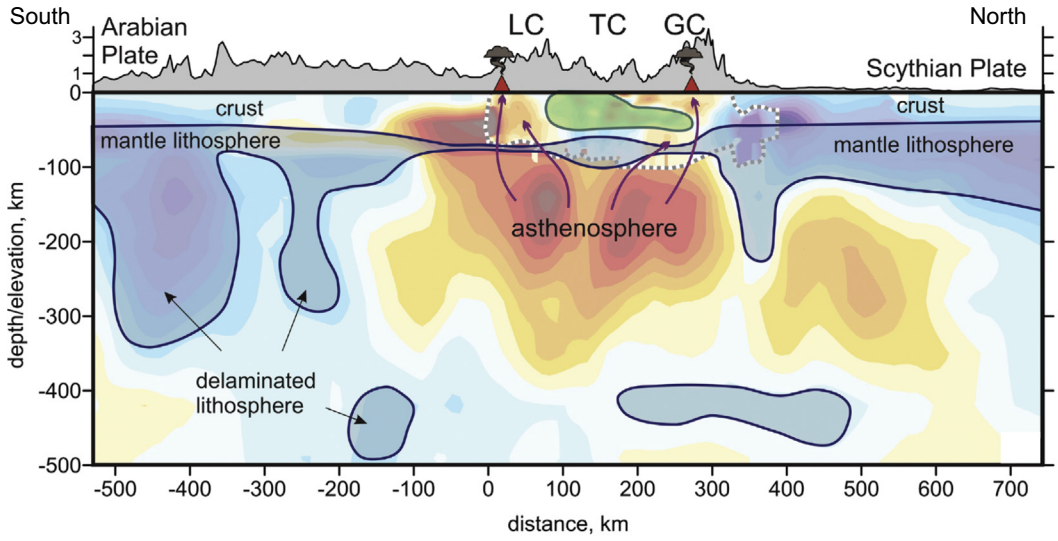

Fig. 8. Combined results of regional and local tomography along a north–south section crossing the Greater (GC) and the Lesser Caucasus (LC) (from Ismail-Zadeh et al., 2020, modified). Bluish patterns indicate the mantle lithosphere; the green pattern outlines the rigid block in Transcaucasia (TC). Arrows indicate possible feeding paths of the volcanic centers. (For interpretation of the references to colour in this figure legend, the reader is referred to the web version of this article.)

From a broader perspective, there is ample thermochronologic evidence of increased cooling/exhumation starting in the Middle-to-Late Miocene over a wide area stretching -west to east- from the eastern Pontides of NE Turkey, across the AT fold-and-thrust belt of Georgia, to the Lesser Caucasus of Armenia and Azerbaijan (Albino et al., 2014; Cavazza et al., 2017, 2019; Gusmeo et al., 2021). Intraplate strain distribution across the hinterland of the Arabia-Eurasia suture was largely dictated by the geometry and orientation of rift basins and older suture zones. A distinguishable temporal-spatial pattern over such a wide area can be considered to be driven by far-field stresses derived from the Arabia-Eurasia collisional plate interactions. Miocene-to-present tectonic overprinting has largely canceled the thermochronometric memory of older tectonic events except for a few areas like the central Greater Caucasus studied here and small portions of the Lesser Caucasus (Cavazza et al., 2017), where the episodic and incremental nature of intraplate deformation can still be appreciated by integrating multiple thermochronometers.

Neogene inversion of Mesozoic-Paleogene rifts such as the Greater Caucasus and Adjara-Trialeti basins as well as renewed shortening of properly oriented segments of preexisting foldbelts such as the Lesser Caucasus and the eastern Pontides were facilitated by the overall mantle structure of the region. Tomographic studies show that the Caucasian region is squeezed between the Arabian plate to the south and the Eurasian plate to the north, which are displayed in the tomographic models as high-velocity bodies down to a depth of ca. 200–250 km (Fig. 8). A low-velocity anomaly beneath the Greater and Lesser Caucasus has been interpreted as a volume where the mantle lithosphere is thin or altogether missing, thus giving low strength to the lithosphere and favoring strong shortening due to regional collisional processes (Koulakov et al., 2012; Ismail-Zadeh et al., 2020; Cloetingh et al., 2021). Mantle upwelling resulted in weakening of the overlying lithosphere, making it vulnerable to tectonic inversion. It should be noted that mantle upwelling and intraplate deformation by far-field stresses exerted from plate boundaries are not mutually exclusive processes as they often interact or follow up on each other (e.g. Huismans et al., 2001; Burov and Cloetingh, 2009; François et al., 2018).

7. Conclusions

The Arabia-Eurasia collision zone is an ideal region for studying the structural/geodynamic processes inducing intracontinental propagation of deformation in space and time. Here, collision has created a wide zone of diffuse deformation across the Eurasian hinterland, including (i) structural inversion of sedimentary basins, (ii) reactivation of portions of older orogenic sutures, (iii) distributed strike-slip deformation, and (iv) the development of an orogenic plateau. In this area of ongoing collision, the geological record of incremental deformation has not been erased by extreme shortening, thus making possible the reconstruction of the earlier structural history.

The southern Caucasian region has been affected by successive phases of intraplate rifting, quiescence, and inversion. The combined application of multiple low-temperature thermochronometers, maximum temperature determinations, and stratigraphic observations shows that the structural inversion of the central part of the Greater Caucasus rift basin was punctuated by two episodes of cooling/exhumation. A Late Cretaceous - Paleocene episode is recognized here for the first time and resulted from the accretion of the Anatolide-Tauride-Armenian block along the southern Eurasian margin, an event which triggered widespread intraplate deformation in the hinterland of the collision zone. The second episode started in the mid-Miocene, coevally with the docking of the northern Arabian plate. During both events, episodic plate-boundary processes (terrane accretion) produced geologically short-lived stresses (“traumatic stresses”; Stephenson et al., 2020) elastically transmitted into the plate interior, where they were relaxed by permanent non-elastic response like the compressional reactivation of preexisting faults, including basin inversion, in those areas where inherited heterogeneities were favorably arranged. The result is a complex array of various intraplate structural domains with varying degrees of deformation as the detailed tectonic evolution of individual intra-continental areas largely depended on their orientations/positions in relation to the stress generating orogenic processes at the continental margin.

The results of this study place cogent constraints on the tectono-structural evolution of the central Greater Caucasus. It would be tempting to extrapolate these results to the entire orogenic belt but, considering its dimensions and non-cylindrical structural configuration, they should be extended with caution to its other sectors.

CRediT authorship contribution statement

William Cavazza: Conceptualization, Investigation, Resources, Supervision, Writing – original draft, Writing – review & editing. **Thomas Gusmeo:** Conceptualization, Investigation, Data curation, Writing – review & editing. **Massimiliano Zattin:** Investigation, Data curation, Resources, Supervision, Writing – review & editing. **Victor Alania:** Investigation, Resources, Writing – review & editing. **Onise Enukidze:** Investigation, Resources, Writing – review & editing. **Sveva Corrado:** Investigation, Data curation, Resources. **Andrea Schito:** Investigation, Data curation, Resources, Writing – review & editing.

Declaration of Competing Interest

The authors declare that they have no known competing financial interests or personal relationships that could have appeared to influence the work reported in this paper.

Acknowledgments

Discussions and/or fieldtrips with S. Adamia (Inst. of Geophysics, Tbilisi), G. Galoyan (Acad. of Sciences, Yerevan), N. Imamverdiyev (Baku State Univ.), R. Melkonyan (Acad. of Sciences, Yerevan), J. Mosar (Univ. of Fribourg), A.I. Okay (Istanbul Technical Univ.), N. Sadradze (Inst. of Geology, Tbilisi), G. Topuz (Istanbul Technical Univ.), and S. Vincent (CASP, Cambridge) were essential for introducing the senior author to the geology of the Greater and Lesser Caucasus. Reviews of the original submission by Gabor Tari (OMV, Vienna) and an anonymous reviewer greatly improved the manuscript. We thank Irene Albino and Silvia Cattò for laboratory help. This study was funded by a PRIN 2017-2020 grant from the Italian Ministry of University and Research (MUR).

Appendix A. Supplementary data

Supplementary data to this article can be found online at https://doi.org/10.1016/j.gsf.2023.101737.

References

Adamia, S.A., Akhvlediani, K.T., Kilasonia, V.M., Nairn, A.E.M., Papava, D., Patton, D. K., 1992. Geology of the republic of Georgia: a review. Int. Geol. Rev. 34, 447–476.

Adamia, S., Alania, V., Chabukiani, A., Chichua, G., Enukidze, O., Sadradze, N., 2010. Evolution of the Late Cenozoic basins of Georgia (SW Caucasus): a review. Geological Society, London, Special Publication 340, 239–259.

Adamia, S.A., Chkhotua, T., Kekelia, M., Lordkipanidze, M., Shavishvili, I., Zakariadze, G., 1981. Tectonics of the Caucasus and adjoining regions: implications for the evolution of the Tethys ocean. J. Struct. Geol. 3, 437–447. https://doi.org/10.1016/0191-8141(81)90043-2.

Adamia, S., Zakariadze, G., Chkhotua, T., Sadradze, N., Tsereteli, N., Chabukiani, A., Gventsadze, A., 2011. Geology of the Caucasus: a review. Turkish J. Earth Sci. 20, 489–544.

Alania, V., Beridze, T., Enukidze, O., Chagelishvili, R., Lebanidze, Z., Maqadze, D., 2021. The Geometry of the two orogens convergence and collision zones in central Georgia: new data from seismic reflection profiles. In: Bonali, F.L., Pasquarè Mariotto, F.A., Tsereteli, N. (Eds.), Building Knowledge for Geohazard Assesment and Management in the Caucasus and Other Regions. Springer, Dordrecht, pp. 73–88.

Alania, V.M., Chabukiani, A.O., Chagelishvili, R.L., Enukidze, O.V., Gogrichiani, K.O., Razmadze, A.N., Tsereteli, N.S., 2017. Growth structures, piggy-back basins and growth strata of the Georgian part of the Kura foreland fold–thrust belt: implications for Late Alpine kinematic evolution. Geological Society, London, Special Publication 428, 171–185.

Albino, I., Cavazza, W., Zattin, M., Okay, A.I., Adamia, S., Sadradze, N., 2014. Far-field tectonic effects of the Arabia-Eurasia collision and the inception of the North Anatolian Fault system. Geol. Mag. 151, 372–379.

Allen, M.B., Armstrong, H.A., 2008. Arabia-Eurasia collision and the forcing of mid-Cenozoic global cooling. Palaeogeography, Palaeoclimatology, Palaeoecology 265, 52–58.

Avdeev, B., 2011. Tectonics of Greater Caucasus and the Arabia-Eurasia orogen. University of Michigan, p. 147 p.. Ph.D thesis.

Avdeev, B., Niemi, N.A., 2011. Rapid Pliocene exhumation of the central Greater Caucasus constrained by low-temperature thermochronometry. Tectonics 30, TC2009. https://doi.org/10.1029/2010TC002808.

Banks, C.J., Robinson, A.G., Williams, M.P., 1997. Structure and Regional Tectonics of the Achara-Trialet Fold Belt and the Adjacent Rioni and Kartli Foreland Basins, Republic of Georgia. AAPG Memoir 68: Regional and Petroleum Geology of the Black Sea and Surrounding Region 331–346.

Barrier, E., Vrielynck, B., Brouillet, J.-F., Brunet, M.F., 2018. Darius Programme paleotectonic reconstruction of the central Tethyan realm. Commission for the Geological Map of the World, Paris.

Bazhenov, M.L., Burtman, V.S., 2002. Eocene paleomagnetism of the Caucasus (southwest Georgia): Oroclinal bending in the Arabian syntaxis. Tectonophysics 344, 247–259. https://doi.org/10.1016/S0040-1951(01)00189-5.

Bewick, S., Parkinson, I.J., Harris, N., Adamia, S., Sadradze, N., Allen, M.B., Hammond, S., 2022. Quaternary collision-zone magmatism of the Greater Caucasus. J. Petrol. 63, 1–31.

Bird, P., Toksöz, M.N., Sleep, N.H., 1975. Thermal and mechanical models of continent-continent convergence zones. J. Geophys. Res. 80, 4405–4416.

Blackbourn, G.A., Tevzadze, N., Janiashvili, A., Enukidze, O., Alania, V., 2021. South Caucasus palaeogeography and prospectivity: elements of petroleum systems from the Black Sea to the Caspian. J. Petrol. Geol. 44, 237–257.

Bochud, M., 2011. Tectonics of the Eastern Greater Caucasus in Azerbaijan. University of Fribourg, p. 207 p.. Ph.D thesis.

Burov, E., Cloetingh, S., 2009. Controls of mantle plumes and lithospheric folding on modes of intraplate continental tectonics: differences and similarities. Geophysical Journal International 178, 1691–1722.

Cavazza, W., Albino, I., Zattin, M., Galoyan, G., Imamverdiyev, N., Melkonyan, R., 2017. Thermochronometric evidence for Miocene tectonic reactivation of the Sevan-Akera suture zone (Lesser Caucasus): a far-field tectonic effect of the Arabia-Eurasia collision? In: Sosson, M., Stephenson, R.A., Adamia, S.A. (Eds.), Tectonic Evolution of the Eastern Black Sea and Caucasus. Geological Society of London, 428. Special Publication, pp. 187–198. https://doi.org/10.1144/SP428.4.

Cavazza, W., Cattò, S., Zattin, M., Okay, A.I., Reiners, P., 2018. The Miocene Arabia-Eurasia collision zone of southeastern Turkey. Geosphere 4, 513–529. https://doi.org/10.1130/GES01637.1.

Cavazza, W., Albino, I., Galoyan, G., Zattin, M., Cattò, S., 2019. Continental accretion and incremental deformation in the thermochronologic evolution of the Lesser Caucasus. Geosci. Front. 10, 2189–2202. https://doi.org/10.1016/j.gsf.2019.02.007.

Cloetingh, S., 1988. Intraplate stresses: a new element in basin analysis. In: Kleinspehn, K.L., Paola, C. (Eds.), New Perspectives in Basin Analysis. Springer Verlag, New York, pp. 205–230.

Cloetingh, S., Koptev, A., Kovács, I., Gerya, T., Beniest, A., Willingshofer, E., Ehlers, T. A., Andric-Tomaseic, N., Botsyun, S., Eizenhofer, P:R:, François, T., Beekman, F., 2021. Plume-induced sinking of intracontinental lithospheric mantle: An overlooked mechanism of subduction initiation? Geochem. Geophy. Geosy. 22, e2020GC009482.

Cloetingh, S.A.P.L., Ziegler, P.A., Beekman, F., Andriessen, P.A.M., Matenco, L., Bada, G., Garcia-Castellanos, D., Hardebol, N., Dèzes, P., Sokoutis, D., 2005. Lithospheric memory, state of stress and rheology: neotectonic controls on Europe's intraplate continental topography. Quaternary Sci. Rev. 24, 241–304.

Corrado, S., Gusmeo, T., Schito, A., Alania, V., Enukidze, O., Conventi, E., Cavazza, W., 2021. Validating far-field deformation styles from the Adjara-Trialeti fold-and-thrust belt to the Greater Caucasus (Georgia) through multi-proxy thermal maturity datasets. Mar. Petrol. Geol. 130, 105141.

Cowgill, E., Forte, A.M., Niemi, N., Avdeev, B., Tye, A., Trexler, C., Javakhishvili, Z., Elashvili, M., Godoladze, T., 2016, Relict basin closure and crustal shortening budgets during continental collision: An example from Caucasus sediment provenance: Tectonics, v. 35, p. 2918–2947, https:// doi .org /10 .1002 / 2016TC004295.

Cowgill, E., Niemi, N.A., Forte, A.M., and Trexler, C.C., 2018. Reply to Comment by Vincent et al. Tectonics 37, 1017–1028. https:// doi .org /10 .1002 / 2017TC004793.

Danišík, M., Sachsenhofer, R.F., Frisch, W., Privalov, V.A., Panova, E.A., Spiegel, C., 2010. Thermotectonic evolution of the Ukrainian Donbas Foldbelt revisited: new constraints from zircon and apatite fission track data. Basin Res. 22, 681–698.

Dewey, J.F., Pitman, W.C., Ryan, W.B., Bonnin, J., 1973. Plate tectonics and the evolution of the Alpine system. Geological Society of America Bulletin 84, 3137–3180.

Ershov, A.V., Brunet, M.F., Nikishin, A.M., Bolotov, S.N., Nazarevich, B.P., Korotaev, M. V., 2003. Northern Caucasus basin: thermal history and synthesis of subsidence models. Sediment. Geol. 156, 95–118.

Forte, A.M., Cowgill, E., Murtuzayev, I., Kangarli, T., Stoica, M., 2013. Structural geometries and magnitude of shortening in the eastern Kura fold-thrust belt, Azerbaijan: Implications for the development of the Greater Caucasus Mountains. Tectonics 32, 688–717. https://doi.org/10.1002/tect.20032.

Forte, A.M., Cowgill, E.S., Whipple, K.X., 2014. Transition from a singly vergent to a doubly vergent wedge in a young orogen: The Greater Caucasus. Tectonics 33, 2077–2101. https://doi.org/10.1002/2014TC003651.

Forte, A.M., Gutterman, K.R., van Soest, M.C., Gallagher, K., 2022. Building a young mountain range: insight into the growth of the Greater Caucasus Mountains from detrital zircon (U-Th)/He thermochronology and 10Be erosion rates. Tectonics 41.

François, T., Koptev, A., Cloetingh, S., Burov, E., Gerya, T., 2018. Plume-lithosphere interactions in rifted margin tectonic settings: Inferences from thermo-mechanical modelling. Tectonophysics 746, 138–154.

Gamkrelidze, I., Okrostsvaridze, A., Maisadze, F., Basheleishvili, L., Boichenko, G., 2019. Main features of geological structure and geotourism potential of Georgia, the Caucasus. Mod. Environ. Sci. Eng. 5, 422–442. https://doi.org/10.15341/mese(2333-2581)/05.05.2019/010.

Gusmeo, T., Cavazza, W., Alania, V.M., Enukidze, O.V., Zattin, M., Corrado, S., 2021. Structural inversion of back-arc basins—The Neogene Adjara-Trialeti fold-and-thrust belt (SW Georgia) as a far-field effect of the Arabia-Eurasia collision. Tectonophysics 803, 228702.

Gusmeo, T., Schito, A., Corrado, S., Alania, V., Enukidze, O., Zattin, M., Pace, P., Cavazza, W., 2022. Tectono-thermal evolution of central Transcaucasia: Thermal modelling, seismic interpretation, and low-temperature thermochronology of the eastern Adjara-Trialeti and western Kura sedimentary basins (Georgia). J. Asian Earth Sci. 237, 105355. Hempton, M.R., 1985. Structure and deformation history of the Bitlis suture near Lake Hazar, southeastern Turkey. Geol. Soc. Am. Bull. 96, 233–243.

Huismans, R.S., Podladchikov, Y.Y., Cloetingh, S., 2001. Transition from passive to active rifting: Relative importance of asthenospheric doming and passive extension of the lithosphere. J. Geophys. Res. Solid Earth 106, 11271–11291.

Ismail-Zadeh, A., Adamia, S., Chabukiani, A., Chelidze, T., Cloetingh, S., Floyd, M., 2020. Geodynamics, seismicity, and seismic hazards of the Caucasus. Earth-Sci. Rev. 207, 103222.

Jess, S., Stephenson, R., Roberts, D.H., Brown, R., 2020. Reply to: Thermal history solutions from thermochronology must be governed by geological relationships: A comment on Jess et al. (2019). Geomorphology 360, 106971.

Karakhanyan, A., Vernant, P., Doerflinger, E., Avagyan, A., Philip, H., Aslanyan, R., Masson, F., 2013. GPS constraints on continental deformation in the Armenian region and Lesser Caucasus. Tectonophysics 592, 39–45.

Khain, V.E., 1975. Structure and main stages in the tectono-magmatic development of the Caucasus: An attempt at geodynamic interpretation. Am. J. Sci. 275, 131–156.

Knipper, A.L. 1980. The tectonic position of ophiolites of the Lesser Caucasus. In: Panayiotou, A. (Ed.) Proceedings of the International Ophiolite Symposium Cyprus. Geological Survey Department, Nicosia, 372-376.

Kohn, B., Chung, L., Gleadow, A., 2019. Fission-track analysis: filed collection, sample preparation and data acquisition. In: Malusà, M.G., Fitzgerald, P.G. (Eds.), Fission-Track Thermochronology and Its Application to Geology. Springer International Publishing, pp. 25–48. https://doi.org/10.1007/978-3-319-89421-8_3.

Kopp, M.L., Korchemagin, V.A., Kolesnichenko, A.A., 2010. Alpine deformations in Donbass: Periodicity, character of stresses, and their probable sources. Geotectonics 44, 405–423.

Koulakov, I., Zabelina, I., Amanatashvili, I., Meskhia, V., 2012. Nature of orogenesis and volcanism in the Caucasus region based on results of regional tomography. Solid Earth 3, 327–337.

Kral, J., Gurbanov, A.G., 1996. Apatite fission track data from the Great Caucasus pre-Alpine basement. Chemie Der Erde-Geochemistry 56, 177–192.

Malusà, M.G., Fitzgerald, P.G. (Eds.), 2019. Fission-Track Thermochronology and Its Application to Geology. Springer International Publishing, Switzerland.

Maystrenko, Y., Stovba, S., Stephenson, R., Bayer, U., Menyoli, E., Gajewski, D., Huebscher, K., Rabbel, W., Saintot, A., Starostenko, V., Thybo, H., Tolkunov, A., 2003. Crustal-scale pop-up structure in cratonic lithosphere: DOBRE deep seismic reflection study of the Donbas fold belt, Ukraine. Geology 31, 733–736.

McQuarrie, N., van Hinsbergen, D.J., 2013. Retrodeforming the Arabia-Eurasia collision zone: Age of collision versus magnitude of continental subduction. Geology 41, 315–318.

Mosar, J., Kangarli, T., Bochud, M., Glasmacher, U.A., Rast, A., Brunet, M.-F., Sosson, M., 2010. Cenozoic-Recent tectonics and uplift in the Greater Caucasus: a perspective from Azerbaijan, *in* Sosson, M., Kaymakci, N., Stephenson, R.A., Bergerat, F., and Starostenko, V., eds., Sedimentary Basin Tectonics from the

Black Sea and Caucasus to the Arabian Platform. Geological Society of London, Special Publications 340, v. 340, p. 261–280, doi:10.1144/SP340.12.
Mosar, J., Mauvilly, J., Koiava, K., Gamkrelidze, I., Enna, N., Lavrishev, V., Kalberguenova, V., 2022. Tectonics in the Greater Caucasus (Georgia – Russia): From an intracontinental rifted basin to a doubly verging fold-and-thrust belt. Mar. Petrol. Geol. 140. https://doi.org/10.1016/j.marpetgeo.2022.105630.
Mouthereau, F., Lacombe, O., Vergés, J., 2012. Building the Zagros collisional orogen: timing, strain distribution and the dynamics of Arabia/Eurasia plate convergence. Tectonophysics 532, 27–60.
Nemčok, M., Glonti, B., Yukler, A., Marton, B., 2013. Development history of the foreland plate trapped between two converging orogens; Kura Valley, Georgia, case study, *in* Nemčok, M., Mora, A., and Cosgrove, J.W., eds., Thick-Skin-Dominated Orogens: from Initial Inversion to Full Accretion. Geological Society of London, Special Publication 377, 159–188, doi:10.1144/SP377.9.
Oberhänsli, R., Candan, O., Bousquet, R., Rimmele, G., Okay, A., Goff, J., 2010. Alpine high-pressure evolution of the eastern Bitlis complex, SE Turkey. Geological Society, London, Special Publication 340, 461–483.
Okay, A.I., Arman, M.B., Göncüoglu, M.C., 1985. Petrology and phase relations of the kyanite-eclogites from eastern Turkey. Contributions to Mineralogy and Petrology 91, 196–204.
Okay, A.I., Tüysüz, O., 1999. Tethyan sutures of northern Turkey. In: Durand, B., Jolivet, L., Horváth, F., Séranne, M. (Eds.), The Mediterranean Basins: Tertiary Extension within the Alpine Orogen. Geological Society of London, 156. Special Publication, pp. 475–515. https://doi.org/10.1144/gsl.sp.1999.156.01.22.
Okay, A.I., Zattin, M., Cavazza, W., 2010. Apatite fission-track data for the Miocene Arabia-Eurasia collision. Geology 38, 35–38. https://doi.org/10.1130/G30234.1.
Okrostsvaridze, A., Chung, S.L., Chang, Y.H., Gagnidze, N., Boichenko, G., Gogoladze, S., 2018. Zircons U-Pb geochronology of the ore-bearing plutons of Adjara-Trialeti folded zone, Lesser Caucasus and analysis of the magmatic processes. Bulletin of the Georgian National Academy of Sciences 12, 90–99.
Pirouz, M., Avouac, J.P., Hassanzadeh, J., Kirschvink, J.L., Bahroudi, A., 2017. Early Neogene foreland of the Zagros, implications for the initial closure of the Neo-Tethys and kinematics of crustal shortening. Earth and Planetary Science Letters 477, 168–182.
Raimondo, T., Hand, M., Collins, W.J., 2014. Compressional intracontinental orogens: Ancient and modern perspectives. Earth-Science Reviews 130, 128–153.
Reilinger, R., McClusky, S., Vernant, P., Lawrence, S., Ergintav, S., Cakmak, R., Ozener, H., Kadirov, F., Guliev, I. Stepanyan, R. Nadariya, M., Hahubia, G., Mahmoud, Sakr, K., ArRajehi, A., Paradissis, D., Al-Aydrus, A., Prilepin, M., Guseva, T., Evren, E., Dmitrotsa, A., Filikov, S., Gomez, F., Al-Ghazzi, R., Karam, G., 2006. GPS constraints on continental deformation in the Africa-Arabia-Eurasia continental collision zone and implications for the dynamics of plate interactions. J. Geophys. Res. Solid Earth 111, B05411, https://doi.org /10.1029 /2005jb004051.
Robinson, A.G., Rudat, J.H., Banks, C.J., Wiles, R.L.F., 1996. Petroleum geology of the Black Sea. Mar. Petrol. Geol. 13, 195–223.
Saintot, A., Stephenson, R., Brem, A., Stovba, S., Privalov, V., 2003. Paleostress field reconstruction and revised tectonic history of the Donbas fold and thrust belt (Ukraine and Russia). Tectonics 22. https://doi.org/10.1029/2002TC001366.
Saura, E., Garcia-Castellanos, D., Casciello, E., Parravano, V., Urruela, A., Vergés, J., 2015. Modeling the flexural evolution of the Amiran and Mesopotamian foreland basins of NW Zagros (Iran-Iraq). Tectonics 34, 377–395.
Sobornov, K., 2021. Structure and evolution of the Terek-Caspian fold-and-thrust belt: New insights from regional seismic data. J. Petrol. Geol. 44, 259–286.
Sokhadze, G., Floyd, M., Godoladze, T., King, R., Cowgill, E.S., Javakhishvili, Z., Hahubia, G., Reilinger, R., 2018. Active convergence between the Lesser and Greater Caucasus in Georgia: Constraints on the tectonic evolution of the Lesser-Greater Caucasus continental collision. Earth Planet. Sci. Lett. 481, 154–161.
Sosson, M., Rolland, Y., Müller, C., Danelian, T., Melkonyan, R., Kekelia, S., Adamia, S. A., Babazadeh, V., Kangarli, T., Avagyan, A., Galoyan, G., Mosar, J., 2010. Subductions, obduction and collision in the Lesser Caucasus (Armenia, Azerbaijan, Georgia), new insights, *in* Sosson, M., Kaymakci, N., Stephenson, R. A., Bergerat, F., and Starostenko, V., eds., Sedimentary Basin Tectonics from the Black Sea and Caucasus to the Arabian Platform. Geological Society of London, Special Publication 340, 329–352. https://doi.org/10.1144/SP340.14.
Stampfli, G.M., Hochard, C., 2009. Plate tectonics of the Alpine realm. Geological Society of London, Special Publication 327, 89–111.
Stephenson, R.A., Stovba, S.M., Starostenko, V.I., 2001. Pripyat-Dniepr-Donets Basin: implications for dynamics of rifting and the tectonic history of the northern Peri-Tethyan Platform. In: Ziegler, P.A., Cavazza, W., Robertson, A.H.F., Crasquin-Soleau, S. (Eds.), Peri-Tethys Memoir 6: Peri-Tethyan Rift/wrench Basins and Passive Margins. Muséum national d'Histoire naturelle, Paris, pp. 369–406.
Stephenson, R.A., Schiffer, C., Peace, A., Nielsen, S.B., Jess, S., 2020. Late Cretaceous-Cenozoic basin inversion and palaeostress fields in the North Atlantic-western Alpine-Tethys realm: Implications for intraplate tectonics. Earth-Sci. Rev. 210, 103252.
Stovba, S.M., Stephenson, R.A., 1999. The Donbas Foldbelt: its relationships with the uninverted Donets segment of the Dniepr-Donets Basin, Ukraine. Tectonophysics 313, 59–83.
Tari, G., Simmons, M.D., 2018. History of deepwater exploration in the Black Sea and an overview of deepwater petroleum play types. Geological Society, London, Special Publications 464, 439–475.
Tari, G., Vakhania, D., Tatishvili, G., Mikeladze, V., Gogritchiani, K., Vacharadze, S., Mayer, J., Sheya, C., Siedl, W., Banon, J.J.M., Trigo Sanchez, J.L., 2018. Stratigraphy, structure and petroleum exploration play types of the Rioni Basin, Georgia. Geological Society, London, Special Publications 464, 403–438.
Tari, G., Vrsic, A., Gumpenberger, T., Mekonnen, E., Hujer, W., Fallah, M., Tevzadze, N., Janiashvili, A., Pace, P., Ricciato, A., Alania, V., Enukidze, O., 2021. Eocene volcaniclastics in the Kartli Basin, Georgia: a fractured reservoir sequence. J. Petrol. Geol. 44, 413–434.
Trexler, C.C., Cowgill, E., Niemi, N.A., Vasey, D.A., Godoladze, T., 2022. Tectonostratigraphy and major structures of the Georgian Greater Caucasus: Implications for structural architecture, along-strike continuity, and orogen evolution. Geosphere 17, 1–30. https://doi.org/10.1130/GES02385.1.
Turner, J.P., Williams, G.A., 2004. Sedimentary basin inversion and intraplate shortening. Earth Sci. Rev. 65, 277–304.
Tye, A.R., Niemi, N.A., Cowgill, E., Kadirov, F.A., Babayev, G.R., 2022. Diverse deformation mechanisms and lithologic controls in an active orogenic wedge: Structural geology and thermochronometry of the eastern Greater Caucasus. Tectonics 41.
Vasey, D.A., Cowgill, E., Roeske, S.M., Niemi, N.A., Godoladze, T., Skhirtladze, I., Gogoladze, S., 2020. Evolution of the Greater Caucasus basement and formation of the Main Caucasus Thrust. Georgia. Tectonics 39. https://doi.org/10.1029/2019TC005828.
Vincent, S.J., Morton, A.C., Carter, A., Gibbs, S., Barabadze, T.G., 2007. Oligocene uplift of the Western Greater Caucasus: An effect of initial Arabia-Eurasia collision. Terra Nova 19, 160–166. https://doi.org/10.1111/j.1365-3121.2007.00731.x.
Vincent, S.J., Carter, A., Lavrishchev, V.A., Rice, S.P., Barabadze, T.G., Hovius, N., 2011. The exhumation of the western Greater Caucasus: A thermochronometric study. Geol. Mag. 148, 1–21. https://doi.org/10.1017/S0016756810000257.
Vincent, S.J., Braham, W., Lavrishchev, V.A., Maynard, J.R., Harland, M., 2016. The formation and inversion of the western Greater Caucasus Basin and the uplift of the western Greater Caucasus: Implications for the wider Black Sea region. Tectonics 35, 2948–2962. https://doi.org/10.1002/2016TC004204.
Vincent, S.J., Saintot, A., Mosar, J., Okay, A.I., Nikishin, A.M., 2018. Comment on "Relict basin closure and crustal shortening budgets during continental collision: An example from Caucasus sediment provenance" by Cowgill et al. (2016). Tectonics 37, 1006–1016, https:// doi .org /10 .1002 /2017TC004515.
Vincent, S.J., Somin, M.L., Carter, A., Vezzoli, G., Fox, M., Vautravers, B., 2020. Testing models of Cenozoic exhumation in the Western Greater Caucasus. Tectonics 39, 1–27. https://doi.org/10.1029/2018tc005451.
Yılmaz, Y., 1993. New evidence and model on the evolution of the southeast Anatolian orogen. Geological Society of America Bulletin 105, 251–271.
Yılmaz, A., Adamia, S.A., Yılmaz, H., 2014. Comparisons of the suture zones along a geotraverse from the Scythian Platform to the Arabian Platform. Geosci. Front. 5, 855–875. https://doi.org/10.1016/j.gsf.2013.10.004.
Yılmaz, A., Adamia, S.A., Chabukiani, A., Chkhotua, T., Erdogan, K., Tuzcu, S., Karabiyikoglu, M., 2000. Structural correlation of the southern Transcaucasus (Georgia)-eastern Pontides (Turkey). In: Bozkurt, E., Winchester, J.A., Piper, J.D. A. (Eds.), Tectonics and Magmatism in Turkey and the Surrounding Area, vol. 173. Geological Society of London, Special Publications, 171–182.
Zabelina, I., Koulakov, I., Amanatashvili, I., El Khrepy, S., Al-Arifi, N., 2016. Seismic structure of the crust and uppermost mantle beneath Caucasus based on regional earthquake tomography. J Asian Earth Sci. 119, 87–99.
Ziegler, P.A., 1987. Late Cretaceous and Cenozoic intra-plate compressional deformations in the Alpine foreland - a geodynamic model. Tectonophysics 137, 389–420.
Ziegler, P.A., Cloetingh, S., van Wees, J.-D., 1995. Dynamics of intraplate compressional deformation: the Alpine foreland and other examples. Tectonophysics 252, 7–59.
Zonenshain, L.P., Le Pichon, X., 1986. Deep basins of the Black Sea and Caspian Sea as remnants of Mesozoic back-arc basins. Tectonophysics 123, 181–211.